

The H1 detector at HERA

H1 Collaboration

I. Abt^h, T. Ahmed^d, S. Aidⁿ, V. Andreev^z, B. Andrieu^{ac}, R.-D. Appuhn^l, C. Arnault^{ab},
M. Arpagaus^{ak}, A. Babaev^y, H. Bärwolff^{aj}, J. Bán^r, E. Banas^{g,l}, P. Baranov^z,
E. Barrelet^{ad}, W. Bartel^l, M. Barth^e, U. Bassler^{ad}, F. Basti^{ag}, D.E. Baynham^f, J.-M. Baze^j,
G.A. Beck^u, H.P. Beck^{al}, D. Bederede^j, H.-J. Behrend^l, C. Beigbeder^{ab}, A. Belousov^z,
Ch. Berger^a, H. Bergstein^a, R. Bernard^j, G. Bernardi^{ad}, R. Bernet^{ak}, R. Bernier^{ab},
U. Berthon^{ac}, G. Bertrand-Coremans^e, M. Besançon^j, R. Beyer^l, J.-C. Biasci^{ab},
P. Biddulph^w, V. Bidoli^{ag}, E. Binder^l, P. Binko^l, J.-C. Bizot^{ab}, V. Blobelⁿ, F. Blouzon^{ad},
H. Blume^{aa}, K. Borrásⁱ, V. Boudry^{ac}, C. Bourdarios^{ab}, F. Brasse^l, W. Braunschweig^a,
D. Breton^{ab}, H. Brettel^{aa}, V. Brisson^{ab}, D. Bruncko^r, C. Brune^p, U. Buchnerⁱ,
L. Büngenerⁿ, J. Bürger^l, F.W. Büslerⁿ, A. Buniatian^{l,1}, S. Burke^t, P. Burmeister^l,
A. Busata^{ac}, G. Buschhorn^{aa}, A.J. Campbell^k, T. Carli^{aa}, F. Charles^{ad}, M. Charlet^l,
R. Chase^{ab}, D. Clarke^f, A.B. Clegg^s, M. Colomboⁱ, V. Commichau^b, J.F. Connolly^f,
U. Cornett^l, J.A. Coughlan^f, A. Courau^{ab}, M.-C. Cousinou^x, Ch. Coutures^j, A. Coville^{ad},
G. Cozzika^{j,*}, D.A. Cragg^f, L. Criegee^l, H.I. Cronström^v, N.H. Cunliffe^f, J. Cvach^{ac},
A. Cyz^g, S. Dagoret^{ad}, J.B. Dainton^t, M. Danilov^y, A.W.E. Dann^w, D. Darvill^b,
W.D. Dau^q, J. David^{ad}, M. David^j, R.J. Day^f, E. Deffur^l, B. Delcourt^{ab}, L. Del Buono^{ad},
F. Descamps^{ad}, M. Devel^{ab}, J. P. Dewulf^e, A. De Roeck^l, P. Dingus^{ac}, K. Djidi^j,
C. Dollfus^{al}, J.D. Dowell^d, H.B. Dreis^b, A. Drescherⁱ, U. Dretzlerⁱ, J. Duboc^{ad},
A. Ducorps^{ab}, D. Düllmannⁿ, O. Düngerⁿ, H. Duhm^{m,†}, B. Dulny^{aa}, F. Dupont^{ab},
R. Ebbinghausⁱ, M. Eberle^m, J. Ebert^{ai}, T.R. Ebert^t, G. Eckerlin^l, B.W.H. Edwards^f,
V. Efremenko^y, S. Egli^{al}, S. Eichenberger^{al}, R. Eichler^{ak}, F. Eisele^o, E. Eisenhandler^u,
N.N. Ellis^d, R.J. Ellison^w, E. Elsen^l, A. Epifantsev^y, M. Erdmann^o, W. Erdmann^{ak},
G. Ernstⁱ, E. Evrard^e, G. Falley^l, L. Favart^e, A. Fedotov^y, D. Feekenⁿ, R. Felst^l,
J. Feltesse^j, Z.Y. Feng^{ad}, I.F. Fensome^d, J. Fent^{aa}, J. Ferencei^l, F. Ferrarotto^{ag}, K. Finke^l,
K. Flamm^l, W. Flauger^{l,†}, M. Fleischer^l, M. Flieser^{aa}, P.S. Flower^f, G. Flügge^b,
A. Fomenko^z, B. Fominykh^y, M. Forbush^h, J. Formánek^{af}, J.M. Foster^w, G. Franke^l,
E. Fretwurst^m, W. Fröchtenicht^{aa}, P. Fuhrmann^a, E. Gabathuler^t, K. Gabathuler^{ah},
K. Gadow^l, K. Gamerdinger^{aa}, J. Garvey^d, J. Gayler^l, E. Gažo^l, A. Gellrichⁿ,
M. Gennis^l, U. Gensch^{aj}, H. Genzel^a, R. Gerhards^l, K. Geskeⁿ, I. Giesgen^b,
D. Gillespie^t, W. Glasgow^f, L. Godfrey^h, J. Godlewski^g, U. Goerlach^l, L. Goerlich^g,
N. Gogitidze^z, M. Goldberg^{ad}, A.M. Goodall^t, I. Gorelov^y, P. Goritchev^y, L. Gosset^j,
C. Grab^{ak}, H. Grässler^b, R. Grässler^b, T. Greenshaw^t, C. Gregory^{ac}, H. Greif^{aa},
M. Greweⁱ, G. Grindhammer^{aa}, A. Gruber^{aa}, C. Gruber^q, S. Günther^{aj}, J. Haack^{aj},
M. Haguenaue^{ac}, D. Haidt^l, L. Hajduk^g, D. Hammer^l, O. Hamon^{ad}, M. Hampel^a,
D. Handschuh^l, K. Hangarter^b, E.M. Hanlon^s, M. Hapke^l, U. Harder^{aj}, J. Harjes^l,

P. Hartzⁱ, P.E. Hatton^f, R. Haydar^{ab}, W.J. Haynes^f, J. Heatherington^u, V. Hedberg^v,
 C.R. Hedgecock^f, G. Heinzelmannⁿ, R.C.W. Henderson^s, H. Henschel^{aj}, R. Herma^a,
 I. Herynek^{ae}, W. Hildesheim^{m,ad}, P. Hill^l, D.L. Hill^f, C.D. Hilton^w, J. Hladký^{ae},
 K.C. Hoeger^w, R.B. Hopes^f, R. Horisberger^{ah}, A. Hrisoho^{ab}, J. Huber^{aa}, Ph. Huet^e,
 H. Hufnagel^o, N. Huot^{ad}, J.-F. Huppert^{ad}, M. Ibbotson^w, D. Imbault^{ad}, H. Itterbeck^a,
 M.-A. Jabiol^j, A. Jacholkowska^{ab}, C. Jacobsson^v, M. Jaffré^{ab}, T. Jansen^l, P. Jean^{ab},
 J. Jeanjean^{ab}, L. Jönsson^v, K. Johannsenⁿ, D.P. Johnson^e, L. Johnson^s, P. Jovanovic^d,
 H. Jung^b, P.I.P. Kalmus^u, D. Kant^u, G. Kantel^l, S. Karstensen^{f,l}, S. Kasarian^l,
 R. Kaschowicz^b, P. Kasselmann^m, U. Kathage^q, H.H. Kaufmann^{aj}, G. Kemmerling^b,
 I.R. Kenyon^d, S. Kermiche^x, C. Keuker^a, C. Kiesling^{aa}, M. Klein^{aj}, C. Kleinwortⁿ,
 G. Knies^l, W. Ko^h, T. Kobler^{aa}, J. Koch^m, T. Köhler^a, J. Köhne^{aa}, M. Kolanderⁱ,
 H. Kolanoski^c, F. Kole^h, J. Koll^l, S.D. Kolya^w, B. Koppitzⁿ, V. Korbel^l, M. Kornⁱ,
 P. Kostka^{aj}, S.K. Kotelnikov^z, M.W. Krasny^{g,ad}, H. Krehbiel^l, F. Krivan^r, D. Krücker^b,
 U. Krüger^l, U. Krüner-Marquis^l, M. Kubantsev^y, J.P. Kubenka^{aa}, T. Külper^l, H.-J. Küsel^l,
 H. Küster^b, M. Kuhlen^{aa}, T. Kurča^r, J. Kurzhöferⁱ, B. Kuznik^{ai}, B. Laforge^j,
 F. Lamarche^{ac}, R. Lander^h, M.P.J. Landon^u, W. Lange^l, W. Lange^{aj}, R. Langkau^m,
 P. Lanius^{aa}, J.-F. Laporte^j, L. Laptin^y, H. Laskus^{aa}, A. Lebedev^z, M. Lemler^{g,l},
 U. Lenhardtⁱ, A. Leuschner^l, C. Leverenz^l, S. Levonian^{l,z}, D. Lewin^l, Ch. Ley^b,
 A. Lindnerⁱ, G. Lindström^m, F. Linsel^l, J. Lipinskiⁿ, B. Liss^l, P. Loch^l, A.B. Lodge^f,
 H. Lohmander^v, G.C. Lopez^u, J.-P. Lottin^j, V. Lubimov^y, K. Ludwig^l, D. Lüers^{aa,†},
 N. Lugetski^y, B. Lundberg^v, K. Maeshima^h, N. Magnussen^{ai}, E. Malinovski^z, S. Mani^h,
 P. Marage^e, J. Marks^x, R. Marshall^w, J. Martens^{ai}, F. Martin^{ad}, G. Martin^{ab}, R. Martin^t,
 H.-U. Martyn^a, J. Martyniak^g, V. Masbender^l, S. Masson^b, A. Mavroidis^u, S.J. Maxfield^t,
 S.J. McMahon^t, A. Mehta^w, K. Meier^p, J. Meissner^{aj}, D. Mercer^w, T. Merz^l,
 C.A. Meyer^{al}, H. Meyer^{ai}, J. Meyer^l, S. Mikocki^{g,ab}, J.L. Mills^f, V. Milone^{ag,†}, J. Möck^{aa},
 E. Monnier^{ad}, B. Montés^{ac}, F. Moreau^{ac}, J. Moreels^e, B. Morgan^u, J.V. Morris^f,
 J.M. Morton^t, K. Müller^{al}, P. Murín^r, S.A. Murray^w, V. Nagovizin^y, B. Naroskaⁿ,
 Th. Naumann^{aj}, P. Nayman^{ad}, A. Nepepivo^y, P. Newman^d, D. Newman-Coburn^u,
 D. Newton^s, D. Neyret^{ad}, H.K. Nguyen^{ad}, F. Niebergallⁿ, C. Niebuhr^l, R. Nisius^a,
 T. Novák^{ae}, H. Nováková^{ae}, G. Nowak^g, G.W. Noyes^f, M. Nyberg^v, H. Oberlack^{aa},
 U. Obrockⁱ, J.E. Olsson^l, J. Olszowska^{g,l}, S. Orenstein^{ac}, F. Ould-Saadaⁿ, P. Pailler^j,
 S. Palanque^j, E. Panaro^l, A. Panitch^e, J.-Y. Parey^{ac}, C. Pascaud^{ab}, G.D. Patel^t, A. Patoux^j,
 C. Paulot^{ab}, U. Pein^m, E. Peppel^l, E. Perez^j, P. Perrodo^{ac}, A. Perus^{ab}, S. Peters^{aa},
 J.-P. Pharabod^{ac}, H.T. Phillips^d, J.P. Phillips^w, Ch. Pichler^m, A. Pieuchot^x, W. Pimpl^{aa},
 D. Pitzl^{ak}, A. Porrovecchio^{ag}, S. Prell^l, R. Prosi^l, H. Quehl^l, G. Rädcl^l, F. Raupach^a,
 K. Rauschnabelⁱ, A. Reboux^{ab}, P. Reimer^{ae}, G. Reinmuth^{ab}, S. Reinshagen^l, P. Ribarics^{aa},
 V. Riech^m, J. Riedlberger^{ak}, H. Riegeⁿ, S. Riessⁿ, M. Rietz^b, S.M. Robertson^d,
 P. Robmann^{al}, P. Röpnack^l, R. Roosen^e, K. Rosenbauer^a, A. Rostovtsev^y, C. Royon^j,
 A. Rudge^h, K. Rüter^{aa}, M. Rudowicz^{aa}, M. Ruffer^m, S. Rusakov^z, V. Rusinov^y,
 K. Rybicki^g, J. Sacton^e, N. Sahlmann^b, E. Sanchez^{aa}, D.P.C. Sankey^f, M. Savitski^{l,y},
 P. Schacht^{aa}, S. Schiekⁿ, N. Schirm^m, S. Schleif^p, P. Schleper^o, W. von Schlippe^u,
 C. Schmidt^l, D. Schmidt^{ai}, G. Schmidtⁿ, W. Schmitz^b, H. Schmücker^{aa}, V. Schröder^l,
 J. Schüttⁿ, E. Schuhmann^{aa}, M. Schulz^l, A. Schwind^{aj}, W. Scobel^m, U. Seehausenⁿ,

F. Sefkow^ℓ, R. Sell^ℓ, M. Seman^r, A. Semenov^y, P. Shatalov^y, V. Shekelyan^y,
 I. Sheviakov^z, H. Shooshtari^{ag}, L.N. Shtarkov^z, G. Siegmund^q, U. Siewert^q, Y. Sirois^{ac},
 A. Sirous^ℓ, I.O. Skillicorn^k, P. Škvařil^{ae}, P. Smirnov^z, J.R. Smith^h, L. Smolik^ℓ, D. Sole^f,
 Y. Soloviev^z, J. Špalek^r, H. Spitzerⁿ, R. von Staaⁿ, J. Staeck^b, P. Staroba^{ae}, J. Štastný^{ae},
 M. Steenbockⁿ, P. Štefan^r, P. Steffen^ℓ, R. Steinberg^b, H. Steiner^{ad}, B. Stella^{ag},
 K. Stephens^w, J. Stier^ℓ, J. Stiewe^p, U. Stösslein^{aj}, J. Strachota^ℓ, U. Straumann^{al},
 A. Strowbridge^f, W. Struczinski^b, J.P. Sutton^d, Z. Szkutnik^ℓ, G. Tappern^f, S. Tapprogge^p,
 R.E. Taylor^{ab,am}, V. Tchernyshov^y, V. Tchudakov^y, C. Thiebaux^{ac}, K. Thiele^ℓ,
 G. Thompson^u, R.J. Thompson^w, I. Tichomirov^y, C. Trenkel^q, W. Tribanek^{aa}, K. Tröger^ℓ,
 P. Truöl^{al}, M. Turiot^{ad}, J. Turnau^g, J. Tutas^o, L. Urban^{aa}, M. Urban^{ac}, A. Usik^z,
 Š. Valkár^{af}, A. Valkárová^{af}, C. Vallée^x, G. Van Beek^e, M. Vanderkelen^e, L. Van Lancker^e,
 P. Van Mechelen^e, A. Vartapetian^{ℓ,1}, Y. Vazdik^z, M. Vecko^{ae}, P. Verrecchia^j, R. Vickⁿ,
 G. Villet^j, E. Vogel^a, K. Wackerⁱ, M. Wagener^{ah}, I.W. Walker^s, A. Waltherⁱ, G. Weberⁿ,
 D. Wegenerⁱ, A. Wegner^{aa}, P. Weissbach^{aa}, H. P.Wellisch^{aa}, L. West^d, D. White^f,
 S. Willard^h, M. Winde^{aj}, G.-G. Winter^ℓ, Th. Wolff^{ak}, L.A. Womersley^t, A.E. Wright^w,
 E. Wunsch^ℓ, N. Wulff^ℓ, B.E. Wyborn^f, T.P. Yiou^{ad}, J. Žáček^{af}, D. Zarbock^m, P. Závada^{ae},
 C. Zeitnitz^m, Z. Zhang^{ab}, H. Ziaeeppour^{ab}, M. Zimmer^ℓ, W. Zimmermann^ℓ, F. Zomer^{ab},
 K. Zuber^p

^a I. Physikalisches Institut der RWTH, Aachen, Germany ²

^b III. Physikalisches Institut der RWTH, Aachen, Germany ²

^c Institut für Physik, Humboldt-Universität, Berlin, Germany ²

^d School of Physics and Space Research, University of Birmingham, Birmingham, UK ³

^e Inter-University Institute for High Energies ULB-VUB, Brussels, Universitaire Instelling Antwerpen, Wilrijk, Belgium ⁴

^f Rutherford Appleton Laboratory, Chilton, Didcot, UK ³

^g Institute for Nuclear Physics, Cracow, Poland ⁵

^h Physics Department and IIRPA, University of California, Davis, California, USA ⁶

ⁱ Institut für Physik, Universität Dortmund, Dortmund, Germany ²

^j CEA, DSM/DAPNIA, CE-Saclay, Gif-sur-Yvette, France

^k Department of Physics and Astronomy, University of Glasgow, Glasgow, UK ³

^ℓ DESY, Hamburg, Germany ²

^m I. Institut für Experimentalphysik, Universität Hamburg, Hamburg, Germany ²

ⁿ II. Institut für Experimentalphysik, Universität Hamburg, Hamburg, Germany ²

^o Physikalisches Institut, Universität Heidelberg, Heidelberg, Germany ²

^p Institut für Hochenergiephysik, Universität Heidelberg, Heidelberg, Germany ²

^q Institut für Reine und Angewandte Kernphysik, Universität Kiel, Kiel, Germany ²

^r Institute of Experimental Physics, Slovak Academy of Sciences, Košice, Slovak Republic ⁷

^s School of Physics and Chemistry, University of Lancaster, Lancaster, UK ³

^t Department of Physics, University of Liverpool, Liverpool, UK ³

^u Queen Mary and Westfield College, London, UK ³

^v Physics Department, University of Lund, Lund, Sweden ⁸

^w Physics Department, University of Manchester, Manchester, UK ³

^x CPPM, Université d'Aix-Marseille II, IN2P3-CNRS, Marseille, France

^y Institute for Theoretical and Experimental Physics, Moscow, Russia

^z Lebedev Physical Institute, Moscow, Russia ⁷

^{aa} Max-Planck-Institut für Physik, München, Germany ²

^{ab} LAL, Université de Paris-Sud, IN2P3-CNRS, Orsay, France

^{ac} LPNHE, Ecole Polytechnique, IN2P3-CNRS, Palaiseau, France

^{ad} LPNHE, Universités Paris VI and VII, IN2P3-CNRS, Paris, France

^{ae} Institute of Physics, Czech Academy of Sciences, Praha, Czech Republic ^{7,9}

^{af} Nuclear Center, Charles University, Praha, Czech Republic ^{7,9}

^{ag} INFN Roma and Dipartimento di Fisica, Università "La Sapienza", Roma, Italy

^{ah} Paul Scherrer Institut, Villigen, Switzerland

^{ai} Fachbereich Physik, Bergische Universität Gesamthochschule Wuppertal, Wuppertal, Germany ²

^{aj} DESY, Institut für Hochenergiephysik, Zeuthen, Germany ²

^{ak} Institut für Teilchenphysik, ETH, Zürich, Switzerland ¹⁰

^{al} Physik-Institut der Universität Zürich, Zürich, Switzerland ¹⁰

^{am} Stanford Linear Accelerator Center, Stanford California, USA

Received 1 July 1996

Abstract

General aspects of the H1 detector at the electron–proton storage ring HERA as well as technical descriptions of the magnet, luminosity system, trigger, slow-control, data acquisition and off-line data handling are given. The three major components of the detector, the tracking, calorimeter and muon detectors, will be described in a forthcoming article. The present paper describes the detector that was used from 1992 to the end of 1994. After this a major upgrade of some components was undertaken. Some performance figures from luminosity runs at HERA during 1993 and 1994 are given.

1. Introduction

The H1 detector described in this paper is one of the two detectors built around the interaction regions of the first ever constructed electron–proton storage ring – HERA at the DESY laboratory in Hamburg, Germany. In this accelerator 27.5 GeV electrons collide with 820 GeV protons at a centre of mass energy of 300 GeV. At HERA a new kinematic region becomes accessible for deep inelastic lepton scattering. Such experiments have played a crucial role in understanding the fundamental forces of nature and in providing first evidence for the pointlike constituents of the nucleons [1]. Compared to previous fixed target conditions, [2], experiments at HERA provide an increase by one order of magnitude in resolving power, with values of the momentum transfer squared Q^2 reaching 4×10^4 GeV², an increase of at least two orders of magnitude. In contrast to previous experiments the unique kinematics at HERA makes it possible to observe the hadronic recoil and to study the weak neutral and charged currents at high momentum transfer.

The extensive discussions of all aspects of HERA physics at the three workshops held before the experimental program started [3–5] led to a detector designed for good identification of leptons (especially electrons), high granularity and resolution for jets and good hermiticity to recognize missing transverse energy. These requirements follow from the

fact that the final states will contain several leptons accompanied by quark and gluon jets. The inclusive measurements of neutral and charged current interactions also demand the best possible hadron calorimeter. In addition electron identification and charged particle reconstruction within jets require a high-resolution, large solid angle tracking system. The efficient use of all these tools must rely on a sophisticated trigger system to overcome the adverse background conditions met at an electron–proton machine.

The differential cross-section measurement at a collider such as HERA requires the reconstruction of kinematic variables as close as possible to the parton level. The most relevant kinematic quantities in the deep inelastic electron scattering process are Q^2 , the fraction x (Bjorken scaling variable) of the proton momentum carried by the struck quark and the fractional energy loss y of the electron. These are given in terms of the energies of the incoming electron E_e , the scattered electron E'_e , the incoming proton E_p , the hadronic recoil jet E_h and the corresponding polar angles θ_e and θ_h (both measured relative to the proton direction $\theta = 0$, positive z -direction) as:

$$Q^2 = 4E_e E'_e \cos^2 \frac{\theta_e}{2},$$

$$x = \frac{Q^2}{4E_e E_p y} = \frac{E_e E'_e (1 + \cos \theta_e)}{E_p (2E_e - E'_e (1 - \cos \theta_e))},$$

$$y \equiv y_e = 1 - \frac{E'_e}{E_e} \sin^2 \frac{\theta_e}{2},$$

$$Q^2 = \frac{E_h^2 \sin^2 \theta_h}{1 - y_h} = \frac{(\sum_{h,i} p_{h,i})^2}{1 - y_h},$$

$$y \equiv y_h = \sum_{h,i} \frac{E_{h,i} - p_{z,h,i}}{2E_e}.$$

Q^2 and x can be reconstructed from measured electron or hadronic quantities or a combination of both. Fig. 1 shows contour plots of fixed θ_e and E'_e in the x, Q^2 plane for $E_e = 30$ GeV and $E_p = 820$ GeV and illustrates the influence of finite angle and energy resolution using the actual design values of the H1 detector. The resolution in Q^2 is determined by the electron energy resolution except for large scattering angles, where the angular resolution becomes the dominant term. The latter term only influences the x resolution for large x

* Corresponding author. Tel.: +33 1 6908 2583, fax: +33 1 6908 6428, e-mail: cozzika@hep.saclay.cea.fr

† Deceased.

¹ Visitor from Yerevan Phys. Inst., Armenia.

² Supported by the Bundesministerium für Bildung, Wissenschaft, Forschung und Technologie, FRG under contract numbers 6AC17P, 6AC47P, 6DO57I, 6HH17P, 6HH27I, 6HD17I, 6HD27I, 6K117P, 6MP17I, and 6WT87P.

³ Supported by the UK Particle Physics and Astronomy Research Council, and formerly by the UK Science and Engineering Research Council.

⁴ Supported by FNRS-NFWO, IISN-IKW.

⁵ Supported by the Polish State Committee for Scientific Research, grant Nos. SPUB/P3/202/94 and 2 PO3B 237 08, and Stiftung fuer Deutsch-Polnische Zusammenarbeit, project no.506/92.

⁶ Supported in part by USDOE grant DE F603 91ER40674.

⁷ Supported by the Deutsche Forschungsgemeinschaft.

⁸ Supported by the Swedish Natural Science Research Council.

⁹ Supported by GA ČR, grant no. 202/93/2423, GA AV ČR, grant no. 19095 and GA UK, grant no. 342.

¹⁰ Supported by the Swiss National Science Foundation.

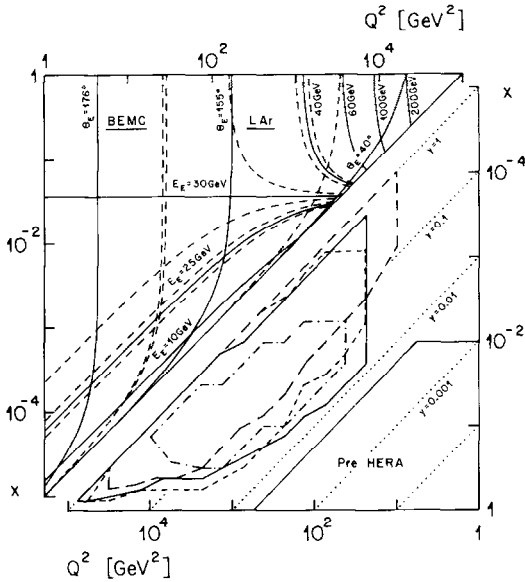


Fig. 1. Top left: contour plots of fixed θ_e and E_c' in the x, Q^2 plane for $E_c = 30$ GeV and $E_p = 820$ GeV. The dashed lines bracketing the isoenergy lines at $E_c' = 30$ and $E_c' = 25$ GeV show the energy resolution of the backward electromagnetic calorimeter (BEMC, $151^\circ < \theta_e < 176^\circ$) at these energies, the dashed lines bracketing the isoenergy line at $E_c' = 40$ GeV the resolution of the liquid argon calorimeter (LAR, $4^\circ < \theta_e < 154^\circ$). Similarly the dashed isoangle lines indicate the angular resolution at $\theta_e = 165^\circ$ and $\theta_e = 90^\circ$, respectively. Bottom right: domains in the Q^2, x plane, where the systematic errors on $d^2\sigma/(dx dQ^2)$ are below 10%. The dotted lines correspond to constant y . The contours correspond to areas where different kinematic reconstruction methods have been used (from Ref. [106]). The area in the lower right corner corresponds to the range accessible to previous experiments.

and small Q^2 . At low y the x resolution is quite poor. The areas in the x, Q^2 plane where a reliable structure function measurement is possible are also indicated in Fig. 1. Here the effects of migration and the systematic errors are also included. Migration is the process where a fraction of events move from one bin in x, Q^2 into a neighbouring bin as a result of measurement errors. For the control of systematic errors the energy calibration, and its stability are of particular importance. Since event rates at high Q^2 are quite low, long term stability is clearly required. Systematic shifts of the outgoing electron energy measurement can generate large shifts in the differential cross-section because there is an amplification factor roughly proportional to y^{-1} , e.g. for $y \approx 0.1, x < 0.5$ an energy shift of 1% results in 10% cross-section change. Since angles are measured both by the calorimeter and the tracker, alignment errors influencing angle measurements are less important.

On the hadron side the above formulae implicitly make use of the Jacquet–Blondel method [6]. It is possible to measure x and Q^2 by using only the outgoing hadrons, without using jet identification or assumptions concerning the proton structure. Furthermore, for HERA kinematics y and Q^2 are more suitably expressed in terms of laboratory variables using the energy-momentum balance between the leptonic

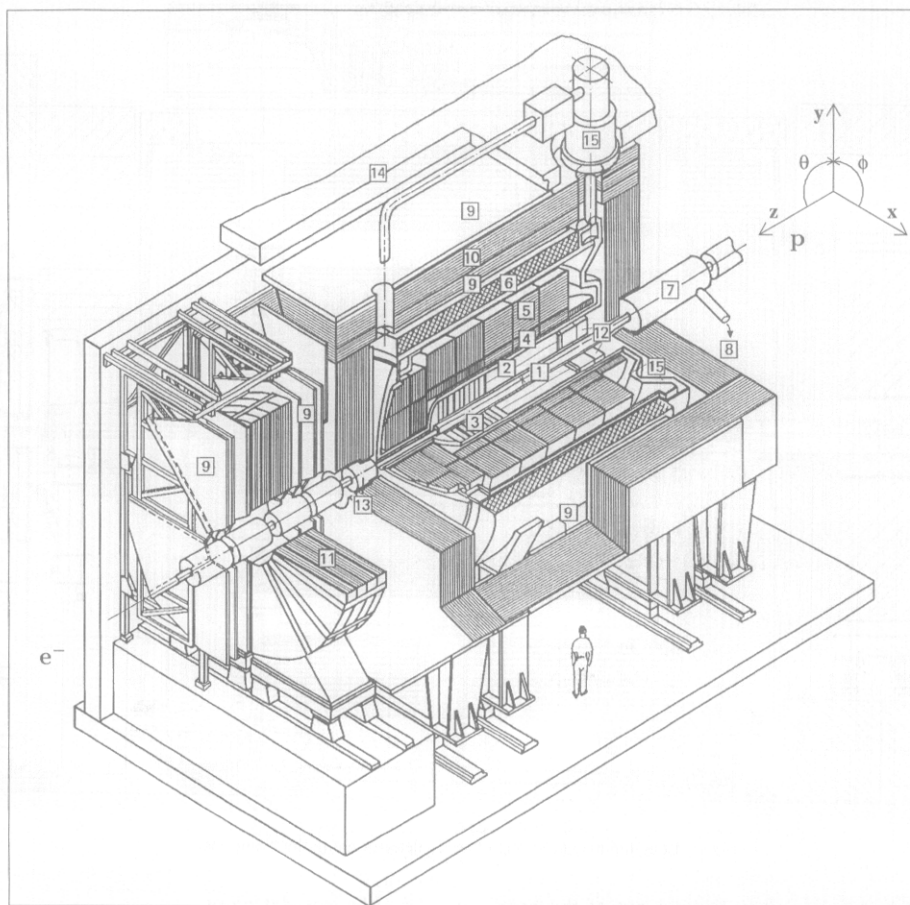
and the hadronic system (as done above) and then deducing x . Because hadrons emitted in the forward direction contribute little to y_h or Q^2 , the unavoidable dead areas along the beam pipe have only a minor impact. Reconstruction errors depend on the size of the beam hole, the uncertainties on the angles and the energies of the outgoing hadrons. Use of the hadron information alone or in combination with the electron information, e.g. by using θ_e and θ_h without direct energy information as in the so-called double angle method [7], extends the measurable regions to considerably lower values of y as shown in Fig. 1.

The largest contribution to the event rates at HERA stems from low Q^2 photoproduction. For example the high cross-section for producing charmed quark-antiquark pairs makes HERA a prolific source of D-mesons with cleaner background conditions than obtained with hadron beams. This makes the study of rare and forbidden decays feasible. The momentum of a tagged $D^{*\pm}$ is correlated with that of the charmed quark produced in γ gluon fusion [7,8] so that the gluon momentum can be reconstructed knowing y_h . Thus the gluon density within the proton may be measured. If forbidden decays such as $D^0 \rightarrow \mu^+\mu^-$ or e^+e^- are to be studied it is important to have good muon identification, and good electron identification at momenta near 1 GeV/c, because the D meson spectrum peaks at rather low energies in particular in the central rapidity region, where these low multiplicity events can be reconstructed.

2. General description of the H1 detector

In the design of the H1 detector prime attention has been given to the clean identification of electrons and to their energy measurement. To facilitate this we opted for a large coil, which encloses the electromagnetic and the hadronic calorimeters. With this choice the amount of dead material in front of the calorimeter and its total weight are minimised. Choosing a liquid argon calorimeter we further benefit from the proven stability of this technique, the ease of its calibration, and the fine granularity which allows to separate electrons from pions to a high degree. Lastly the homogeneity of the response and overall hermiticity are helpful for energy flow measurements as well as missing energy detection. The calorimeter is supplemented by high resolution tracking on the inside and an instrumented iron yoke on the outside for muon detection. In these aspects the H1 detector does not differ strongly from the detectors at e^+e^- colliders, or $p\bar{p}$ colliders built in the past. Specific at HERA are however the high resolution required for hadronic calorimetry as well as the imbalance in the energy of the two colliding beams, which requires an asymmetric detector. Different also is the microstructure of the two beams, which leads to short intervals (96 ns) between two subsequent bunch crossings, and also the high background level, as proton induced background arises from beam line vacuum conditions.

The main elements of the detector are shown in Fig. 2.



| | | | |
|---|---------------------------------|----|--|
| 1 | Beam pipe and beam magnets | 9 | Muon chambers |
| 2 | Central tracking device | 10 | Instrumented iron yoke |
| 3 | Forward tracking device | 11 | Forward muon toroid |
| 4 | Electromagnetic LAr calorimeter | 12 | Backw. electromagn. calorimeter (BEMC) |
| 5 | Hadronic LAr calorimeter | 13 | PLUG calorimeter |
| 6 | Superconducting coil (1.15 T) | 14 | Concrete shielding |
| 7 | Compensating magnet | 15 | Liquid argon cryostat |
| 8 | Helium supply for 7 | | |

Fig. 2. Schematic layout of the H1 detector.

This figure shows as well the reference frame adopted in this experiment.

Since the centre of mass for $e-p$ collisions at HERA is boosted along the proton direction with $\gamma_{cm} = 2.86$ the H1 detector is considerably more massive and highly segmented in this direction. This is apparent from Fig. 3, which shows a cut along the beam axis. In the following we often refer to electron direction as the backward direction (negative z -values relative to the center of the interaction region and $\theta = \pi$), and the proton direction as the forward direction (positive z and $\theta = 0$).

Starting the description outward from the interaction vertex the detector consists of a central and a forward tracking system, each containing different layers of drift chambers and trigger proportional chambers. The liquid argon cryostat surrounds the trackers. It houses the lead absorber plates and readout gaps of the electromagnetic section, which are followed by the steel plates of the hadronic section with their readout gaps. A superconducting cylindrical coil with a diameter of 6 m and a length of 5.75 m provides the analysing field of 1.15 T. The iron return yoke of the magnet is laminated and filled with limited streamer tubes. The

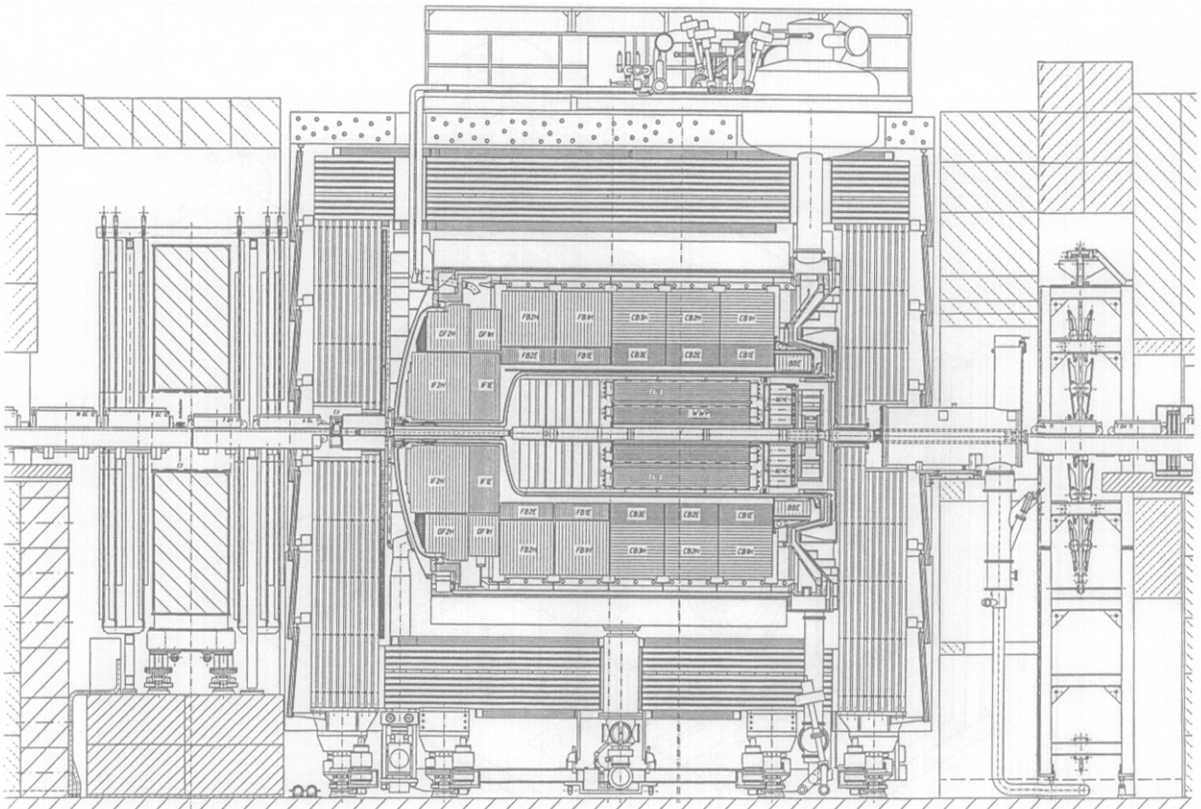


Fig. 3. Longitudinal cut through the H1 detector along the beam line.

small fraction of hadronic energy leaking out of the back of the calorimeter is registered there, and muon tracks are measured. Muon identification further benefits from additional chambers inside and outside of the iron. Stiff muon tracks in the forward direction are analysed in a supplementary toroidal magnet sandwiched between drift chambers. The remaining holes in the liquid argon (LAr) calorimeter are closed with warm calorimeters, a silicon-copper plug at very forward angles, a lead-scintillator calorimeter backed by a tail catcher (part of the muon system) in the backward direction and lastly an electron tagger at $z = -33$ m from the interaction point not shown in Fig. 3. The tagger marks the energy of an electron with very small scattering angle inducing a photoproduction event and, taken in coincidence with a corresponding photon detector at $z = -103$ m upstream from the interaction point, monitors the luminosity by the bremsstrahlung process. Two scintillator walls in backward direction are installed to recognize background produced by the proton beam upstream of the H1 detector. A survey of detector parameters is given in Table 1.

Three of the major components of the detector, the tracking, calorimetry and muon detection systems are not described in this article. Please refer to an article to be published in a forthcoming issue of this journal for a description of these elements (see Ref. [9] or [10]).

2.1. Electron detection

Scattered electrons are observed in the backward electromagnetic calorimeter (BEMC) for $Q^2 \leq 100 \text{ GeV}^2$, in the LAr calorimeter for larger values of Q^2 , and for photoproduction events ($Q^2 \approx 0$) in an electron tagger which is part of the luminosity measuring device.

The BEMC is a conventional lead-scintillator sandwich calorimeter with photodiode readout, providing an energy resolution sampling term of $10\%/\sqrt{E}$. The diodes are located in the ≈ 1 T magnetic field. The backward proportional chamber (BPC) located just in front of the BEMC provides the angular measurement of the electron together with track and vertex data given by the central tracker. The kinematic peak in the energy spectrum of the scattered electron at a value corresponding to the electron beam energy allows a precise overall calibration.

The LAr calorimeter covers the polar angular range $4^\circ \leq \theta \leq 154^\circ$ in a single cryostat. The electromagnetic calorimeter with lead absorber plates of total depth of 20 to 30 radiation lengths provides an energy resolution $\sigma/E \approx 12\%/\sqrt{E}$. Electron identification is based on fine transverse and longitudinal shower shape measurement and a cross-check of the absolute energy calibration of the calorimeters is provided by comparing the calorimetric energy measurement of electrons to the corresponding momentum measure-

Table 1

Summary of H1 detector parameters. Alternatively, design and test beam figures are given in brackets []. Energies are given in GeV.

| Calorimetry | | |
|---------------------------------------|---|-----------------------------------|
| Main calorimeter: liquid argon (LAr) | Electromagnetic part | Hadronic part |
| Granularity | 10 to 100 cm ² | 50 to 2000 cm ² |
| Depth (number of channels) | 20 to 30 X ₀ (30784) | 4.7 to 7 λ _{abs} (13568) |
| Resolution $\sigma(E_{e,h})/E_{e,h}$ | ≈ 11%/√E _c ⊕ 1% | ≈ 50%/√E _h ⊕ 2% |
| Stability of electronic calibration | ≤ 0.2% over one month | |
| LAr purity (decrease of signal) | ≤ 0.2% over one year | |
| Noise per channel | 10 to 30 MeV | |
| Angular coverage – dead channels | 4° < θ < 154° | < 0.3% |
| Backward calorimeter: Pb–scintillator | | |
| Angular coverage – granularity | 151° < θ < 176° | 16 × 16 cm ² |
| Depth – resolution $\sigma(E_c)/E_c$ | 21.7 X ₀ (1 λ _{abs}) | 10%/√E _c ⊕ 1.7 [11%] |
| Tail catcher: iron–streamer tubes | | |
| Angular coverage | 4° < θ < 176° | |
| Depth – resolution $\sigma(E_h)/E_h$ | 4.5 λ _{abs} | 100%/√E _h |
| PLUG calorimeter: Cu Si | | |
| Angular coverage – granularity | 0.7° < θ < 3.3° | 5 × 5 cm ² |
| Depth – resolution $\sigma(E_h)/E_h$ | 4.25 λ (44.6 X ₀) | ≈ 150%/√E _h |
| Electron tagger: Tl(Cl/Br) | | |
| Angular coverage – granularity | θ > 179.7° | 2.2 × 2.2 cm ² |
| Depth – resolution $\sigma(E_c)/E_c$ | 25 X ₀ | ≈ 10%/√E _c ⊕ 1% |
| Tracking | | |
| Coil: radius – field | 3 m – B = 1.15 T, ΔB/B ≤ 2% | |
| Central tracking | | |
| Angular – radial coverage | 25° < θ < 155° | 150 < r < 850 mm |
| Jet chamber: spatial resolution | σ _{rφ} = 170 μm | σ _z = 22.0 mm |
| z-chambers: spatial resolution | σ _{rφ} = 25 and 58 mm | σ _z ≈ 350 μm |
| Momentum – dE/dx resolution | σ _{p/p} < 0.01 [0.003] GeV ⁻¹ | σ(dE)/dE = 10 [6]% |
| Forward/backward tracking | | |
| Angular – radial coverage (f) | 7° < θ < 25° | 120 < r < 800 mm |
| Spatial resolution (f) | σ _{rφ} = 170 μm (σ _r = 29 mm) σ _{x,y} = 210 μm | |
| Angular coverage – resolution (b) | 155° < θ < 175° | σ _{x,y} = 1 mm |
| Trigger proportional chambers | | |
| Angular coverage – channels | 7° < θ < 175° | 3936 |
| Muon detection | | |
| Instrumented iron | | |
| Angular coverage – total area | 4° < θ < 171° | 4000 m ² |
| Number of channels | wires: 103700, strips: 28700, pads: 4000 | |
| Spatial resolution | σ _{wire} = 3–4 mm | σ _{strip} = 10–15 mm |
| Angular – momentum resolution barrel | σ _θ (σ _φ) = 15(10) mrad | [σ _{p/p} ≈ 0.35] |
| Forward muon toroid | | |
| Angular coverage – resolution | 3° < θ < 17° | [0.25 < σ _{p/p} < 0.32] |
| Overall size (x, y, z) – weight | 12 × 15 × 10 m ³ | 2800 t |

ment in the central tracking chambers.

Further electron pion discrimination is available by a dE/dX measurement in the central jet chamber (CJC) and by using the transition radiation detectors incorporated into the forward tracker.

2.2. Hadron and jet detection

The hadronic calorimeter with stainless steel absorber is located within the same cryostat as the electromagnetic calorimeter and supports the latter. Both calorimeters together provide the energy measurements of hadrons. Their total depth ranges between 5 and 7 absorption lengths, de-

pending on the polar angle θ. Events with energy leaking out of the LAr calorimeter are efficiently tagged by the tail catcher consisting of the analog readout of the pads of the limited streamer tube system in the iron instrumentation to improve the calorimeter energy resolution. Measurements in a test beam show that the expected resolution $\sigma/E = 50\%/√E$ has been achieved, with an energy independent term of 2%. Here too combining the calorimetric information with the momentum information from the central tracking chambers provides a cross-check of the absolute energy calibration. Further intercalibration between calorimeters is possible by checking the balance in transverse momentum between the electrons and the hadrons.

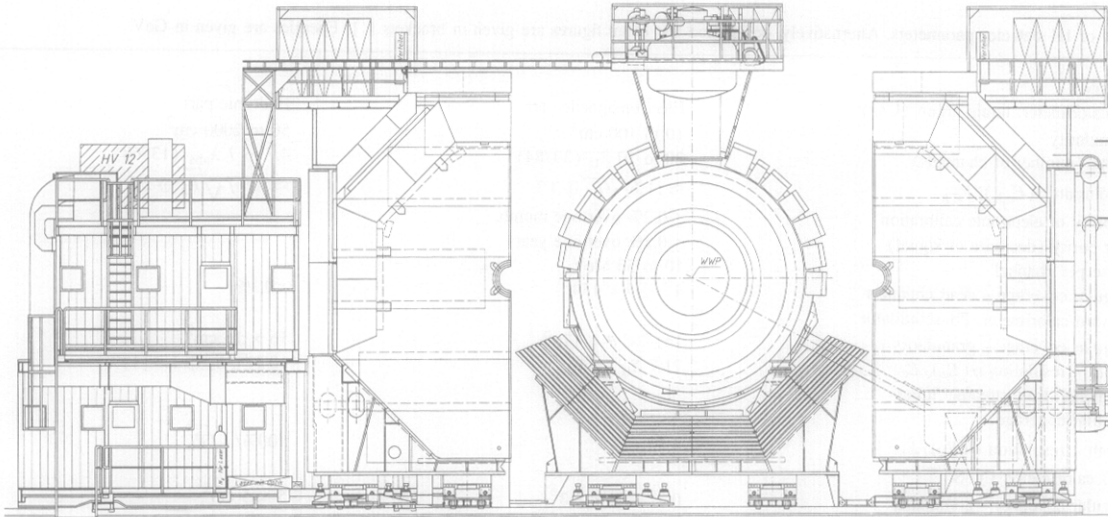


Fig. 4. Front view of the H1 detector with the southern and the northern shells of the iron yoke opened.

Low energy hadrons may also be identified by the dE/dX of the CJC.

2.3. Muon detection

An important source of prompt muons at HERA is semileptonic decays of charm- and bottom mesons, therefore the muon system was designed to identify muons within jets. In the large coil solution of H1 the calorimeter serves to absorb the hadronic activity. It moreover allows to detect penetrating single ionizing tracks while the high field provides sufficient bending power for a momentum measurement. The necessary spatial resolution, matched to the dispersion due to the multiple scattering in the material in front of the instrumented iron, is reached with a total of sixteen streamer tube layers with a basic cell size of $10 \times 10 \text{ mm}^2$, a triple layer each in front and after the iron, a double layer after four iron sheets of 75 mm thickness, and eight single layers in the remaining gaps in between the ten iron sheets. The multiple layers are equipped with pads and cathode strips for the measurement of the coordinate perpendicular to the wires.

In the barrel part muons with energies below 1.2 GeV do not reach the first layer, while muons with energies below 2.0 GeV stop within the iron. In the forward direction the effective threshold is 2.5 GeV, but here the muon energy is usually large enough for muons to traverse all 16 layers of chambers. An independent track segment is then measured which can be linked to forward tracker segments. The comparison between momentum measurement in the tracker and through the muon system reduces misidentification and also allows to discriminate against muons from π and K-decay.

In the extreme forward direction the central tracker and the chamber system in the flux return iron are not adequate for measuring muon momenta with sufficient accuracy. This is why a toroidal magnet with an average field of 1.6 T was

added. The drift chambers are constructed in such a way, that correlated angle and position measurements are possible. This is needed because the hadronic activity from secondary interactions of the target jet is quite high. The spectrometer is useful in the momentum range between 5 and 200 GeV/c. The lower limit is determined by the amount of material traversed, while beyond the upper limit the muon charge can no longer be measured unambiguously.

2.4. HERA beam features

The electron-proton colliding beam facility HERA consists of two independent accelerators storing respectively 820 GeV protons and 27.5 GeV electrons and colliding the two counter-rotating beams head on in four interaction points spaced evenly along its 6.3 km circumference. Electrons are injected at 12 GeV and are guided by a warm magnet system at 0.165 T, while protons are injected at 40 GeV into a ring with superconducting dipole magnets at 4.68 T. The accelerator was designed for 210 circulating bunches with 760 μA protons and 290 μA electrons each [11,12] and a luminosity of $1.5 \times 10^{31} \text{ cm}^{-2}\text{s}^{-1}$. The bunches are separated in time by 96 ns. In the early phases of operation in 1992 and 1993 only 10 and 90 bunches were circulating, respectively. An indication of the HERA performance in 1992, 1993 and 1994 is given in Fig. 6. Since July 1994 the electron beam has been replaced by a positron beam which has considerably improved the beam lifetime at high currents.

Between the last two beam focussing quadrupoles 11.3 m of free space is available for the detector. The beams pass the detector at a height of 5.9 m above floor level ($\approx 20 \text{ m}$ below ground) at an inclination of 5.88 mrad. Presently a 190 mm inner diameter beam pipe is installed, with a wall of 150 μm Al on the inside backed by 2 mm carbon fibre reinforced plastic comprising 1% radiation length. Details of the beam line are shown in Fig. 5. The beam pipe is cooled

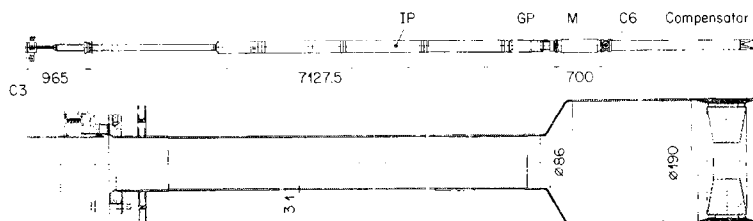


Fig. 5. Cross section of the beam pipe in the H1 detector. IP: interaction point, GP: getter pump, M: beam profile monitor, C6: synchrotron radiation mask (see also Fig. 7). The lower part shows an enlarged view of the forward part with the flexible bellow connections and synchrotron radiation mask C4 (right).

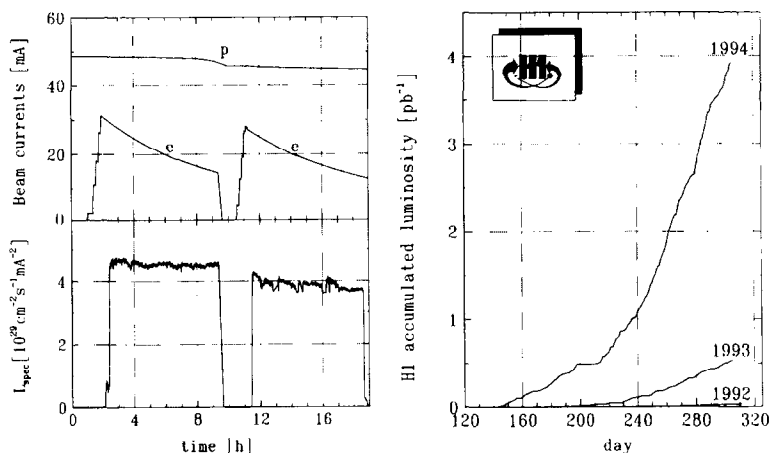


Fig. 6. Performance of the HERA storage ring in the first three years of operation. Left: beam currents (top) and luminosity (bottom) measured during a typical run. Right: integrated luminosity accumulated by H1 over the running periods 1992–1994.

with nitrogen gas, which also circulates on the outside of the central tracker to avoid buildup of larger amounts of inflammable gases leaking from the chambers. Incorporated into the beam pipe are a capacitively coupled proton position monitor [13], synchrotron radiation shielding masks (see below), getter pump connections and a flexible bellow to absorb temperature dependent variations of the beam pipe. For the future upgrade of the tracking near the beam pipe [14,15] a smaller beam pipe with an inner diameter of 90 mm (150 μm Al backed by 0.75 mm carbon fibre) will be installed.

While the radial extension of the beams is small, the finite time spread of the bunches and the zero degree crossing leads to total length of the interaction zone of $\approx \pm 50$ cm. The zero degree crossing was chosen to reduce e–p beam coupling, which could result in beam blow up. Typical vacuum conditions in the beam pipe during the initial running phase lead to a residual gas pressure of $\approx 1\text{--}2 \times 10^{-9}$ hPa primarily consisting of atomic hydrogen and carbon monoxide. Assuming nitrogen as an average representation of the residual gas and a reaction cross-section for protons at 820 GeV ($\sqrt{s} = 39$ GeV) of ≈ 200 mb [16] one expects one proton nitrogen interaction in 10^4 bunch crossings at design luminosity along the interaction region (1 m) compared to one genuine e–p event every 10^5 bunch crossings. The physics rate is dominated by photoproduction giving a visible event

rate of about 200 Hz at design luminosity, the beam gas rate given above corresponds to ≈ 1 kHz. Beam gas background is not restricted to the interaction zone proper and can originate from the whole proton path through the detector. Furthermore beam halo protons hitting apertures contribute, too. Monte Carlo simulations and measurements from the first data taking period indicate roughly a factor 50 higher rate for the latter process than for beam gas events from the interaction zone. These contributions are however more easily removed in the different trigger and filter levels.

The actual tuning of the luminosity optics for the two beams relies partly on the H1 luminosity system. It makes use of the $e p \rightarrow e p \gamma$ bremsstrahlung process and hence is sensitive to electron interactions with the residual gas. By filling both electron and proton bunch sequences in such a way that there is always at least one bunch of each type with no partner for a collision (pilot bunches) background subtraction can be made. During the filling phase the trigger scintillators of the time-of-flight wall can be remotely removed from the beam pipe. The integrated rate in these counters provides an efficient means for monitoring the quality of the beam tune. Only when a lower value for this rate has been reached the counters are moved back in, and the high voltage on all drift and proportional chambers is raised. While proton fill lifetimes well exceeding 24 h have been reached, the lifetime of the electron ring fills during the

HERA startup phase was limited to about 6 h; since July 1994 when positrons were used, this lifetime has increased by a factor ≈ 2 .

2.4.1. Synchrotron radiation shielding

The e^- beam is accompanied by a strong flux of synchrotron radiation photons which are produced in the last bending magnet before the interaction point. Synchrotron radiation from the arcs is absorbed before the H1 detector and need not be considered. At a beam energy of 30 GeV and a stored current of 60 mA we expect a flux of 10^{18} photons per second with an energy above 5 keV into the interaction region. This flux represents a radiated power of 3.6 kW. The critical energy is 42.4 keV. In order to protect the detector elements a system of masks inside the beam pipe is installed.

The synchrotron radiation absorbers were designed such that only photons which have undergone at least two scatterers can reach the central detector region. In order to reduce the photon flux the aperture of the collimators should be as small as possible. The width is thus determined by the requirement for sufficient aperture at injection. Masks which are hit by synchrotron radiation are sources of secondary photons. Therefore the albedo of all surfaces has been reduced by coating the tungsten absorbers with 0.5 mm silver and 0.2 mm copper. For 100 keV photons the albedo is reduced from 10% for pure tungsten to 1% with the appropriate coating. The geometry of the absorbers is shown in Fig. 7. The collimators C_1 , C_2 and C_3 are hit by direct synchrotron light and have to stand a radiated power of about 1 kW each. These collimators are movable and water-cooled. The synchrotron radiation which misses C_3 passes through the detector area and hits an absorber 24 m behind the interaction point. The collimators C_4 , and C_5 have a fixed horizontal aperture of $+30$ mm -25 mm and ± 50 mm, respectively. They protect the detector elements against secondary photons originating from edge scattering at the collimators $C_1 - C_3$ and backscattered photons from the absorber at 24 m. The collimator C_6 is movable and provides an addi-

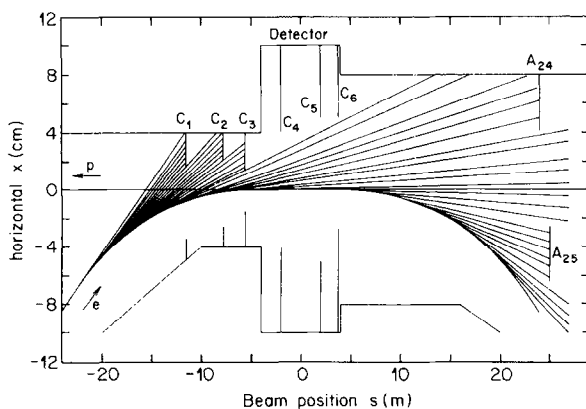


Fig. 7. Arrangement of synchrotron masks shielding the H1 detector from direct synchrotron radiation (from Ref. [107]).

tional shield against photons from 24 m downstream. The aperture can be set between 65 mm and 25 mm with respect to the beam.

The present arrangement of synchrotron radiation masks cuts down the number of photons which enter the central part of the detector to a level of 10^6 photons per second with an energy above 20 keV. Thus at nominal beam conditions we expect about 10^{-1} spurious synchrotron hits in the central tracking chamber per bunch crossing. Due to the low currents and the reduced electron energy of 27.5 GeV we did not observe synchrotron radiation hits in the tracking chambers, consistent with the estimates.

2.5. Detector upgrade

This paper describes the H1 detector as it was up to the end of 1994. During the HERA winter shutdown of 1994–1995 some major upgrade work was done to the detector. It is not the scope of this paper to describe these upgrades, but the subdetectors involved will be enumerated at the end and appropriate references given.

3. Magnet

The magnet consists of a superconducting solenoid and an iron yoke producing an almost uniform field parallel to the HERA beams. The field has only a few percent variation over the region of the tracking chambers. Within that region, 3600 mm in length and 1600 mm in diameter, the field has an average value 1.15 T.

3.1. The iron yoke

The iron yoke has the shape of an octagonal barrel with its axis parallel to the beam axis and to that of the solenoid which it encloses, plus flat end caps. In overall size it is similar to the ALEPH [17] and DELPHI [18] magnets at CERN. The requirements on uniformity of field are less stringent than for those experiments, which have chambers very sensitive to radial field components. Thus reentrant end caps are not needed for the H1 magnet and a much simpler opening mechanism is possible.

The yoke of the H1 magnet is separated into three parts, the northern and southern shells and the base structure (see Fig. 4). The latter consists of the three lower faces of the octagonal barrel, and supports the superconducting coil. The northern and southern shells are mirror images of each other, symmetric about a vertical plane through the beam. Together they form all the rest of the octagonal barrel and the two end caps. Thus each shell is a rigid structure consisting of half of the western endcap and half of the eastern endcap, connected by 2.5 of the 8 faces of the octagonal barrel. Each of the three parts of the iron yoke moves independently on rails.

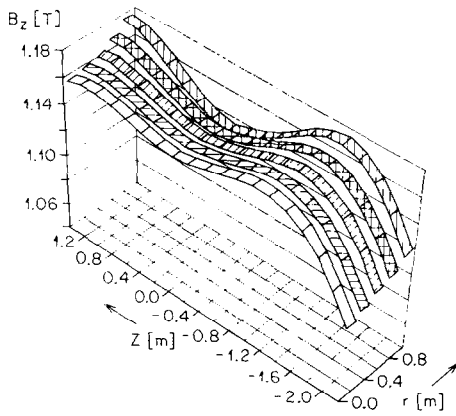


Fig. 8. Main coil field map over the tracking volume. Here z denotes the distance to median plane, see text.

The iron of the octagonal barrel is made of 10 laminations each 75 mm thick, separated by air gaps of 25 mm accommodating a single layer of limited streamer tubes (LST), except for one air gap of 50 mm to accommodate a double layer of LSTs. The iron of the end caps is made up of 10 laminations each of 75 mm, separated by air gaps of 35 mm except for one air gap of 50 mm.

3.2. The superconducting coil

The main solenoid consists of four separate coaxial coils powered in series, symmetrically placed about the median vertical plane. The two coils nearest to the median plane (“central”) are single layers, each of 201 turns, extending from 400 mm to 1420 mm from the median plane. The two coils farthest from the median plane (“peripheral”) are double layers and have each 418 turns, extending from 1520 mm to 2580 mm from the median plane. All four of these windings are housed in one cryogenic envelope with an overall length 5750 mm, inner diameter 5180 mm, outer diameter 6080 mm. The superconductor, bonded into its aluminium substrate, was manufactured in industry [19]. The coils were fabricated from this conductor in modular form of length up to 1.5 m for both double and single layers on a custom built machine using the inside winding technique [20]. Liquid helium is supplied by the central plant at DESY. The parameters of this superconducting coil assembly are given in Table 2.

3.3. The magnetic field measurements

The general similarity in size and shape of the H1 magnet to those of the ALEPH and DELPHI magnets [17,18] made it possible to use the same apparatus for the field measurements throughout a cylindrical volume of radius $r = 1775$ mm and length $L = 5200$ mm. The tracking chambers occupy only a smaller volume ($r = 800$ mm, $L = 3600$ mm, $-1125 < z < 2500$ mm) asymmetric to the median plane of the magnet ($z = 1100$ mm). The axial component B_z

which needs to be known over the tracker volume with an accuracy of 0.3% is shown in Fig. 8 as function of radius and axial distance to the median plane. The average value over the volume is 1.15 T at the nominal magnet current of 5514 A, and the maximum departure from this value is 4.5% at the extreme backward end of the central tracker.

The longitudinal field integral $\int B_z dz$ for the H1 magnet was evaluated to be 8.32 Tm at the nominal current.

3.4. The forward muon toroid

The toroidal magnet for the forward muon detector consists of 8 solid iron modules built into two mobile half-toroids for access purposes. The inner radius of the toroid is 0.65 m, the outer radius 2.90 m, and the length between the flat ends 1.20 m. The weight is 250 tons.

There are 12 coils wound on the toroid, each consisting of 15 turns of water-cooled copper, carrying a current of 150 A. The copper windings are square in cross-section with side 11.5 mm, with a 8.5 mm diameter hole for water-cooling.

The magnetic field within the iron toroid has been measured by the change in flux, as the magnet is turned on or off, through loops of wire threaded through small holes in the iron. The field varies with radius, from 1.75 T at a radius of 0.65 m to 1.5 T at a radius of 2.90 m.

3.5. Compensating magnet

The compensating coil is located at the proton entrance side of the H1 magnet with its center at 4.4 m from the interaction point. Its purpose is to provide a longitudinal field integral $\int B_z dz$ equal and opposite to that of the main H1 magnet. This is required if longitudinal polarization of the electron beam is to be achieved. It also avoids horizontal-vertical coupling and minimises closed orbit shifts in HERA due to any misalignment of the H1 magnet [21]. Its downstream end extends into the endcap of the main magnet. This 1.8 m long superconducting coil was manufactured in industry [22] from NbTi cable embedded into a copper matrix insulated by glass fiber epoxy. The magnetic field is shielded by an iron yoke, with both iron and coil mounted inside a pressure vessel, which is cooled by liquid He from the main DESY transfer line. The relevant parameters are also given in Table 2. The field integral and the magnetic field axis have been determined by means of a rotatable Hall probe described in detail in Ref. [23].

4. Luminosity system and electron tagger

The luminosity system serves several purposes. Its main task is a fast relative luminosity measurement with a statistical precision of $\sim 2\%$ at nominal beam conditions. It also provides electron beam monitoring for the HERA machine, absolute luminosity measurement in the interaction region with an accuracy of $\sim 5\%$, tagging of photoproduction events and energy measurement for electrons scattered

Table 2
Parameters of the superconducting magnets.

| Solenoid parameters | Main H1 magnet | Compensating magnet |
|--------------------------------|--|---------------------------|
| Superconductor | | |
| Dimensions | 26 × 4.5 mm ² | 3.1 × 2.1 mm ² |
| Type | Rutherford cable on high purity Al (RRR 500) substrate | ABB-Zürich cable |
| Length (weight) | 22.5 km (7.7 t) | 4.5/4.5 km (0.49 t) |
| Winding geometry | | |
| # of coils | 2 ("central")/ 2 ("peripheral") | 1 |
| # of layers (turns) | 1 (201)/2 (209) | 14 (534) |
| # of turns: total | 1238 | 7576 |
| Inner radius | 2750/2750 mm | 320 mm |
| Outer radius | 2800/2850 mm | 429 mm |
| Cooling | support cylinder, forced flow | cryostat bath cooled |
| Vacuum chamber | | |
| Inner/outer diameter | 5200/6080 mm | 238/870 mm |
| Length/thickness | 5750/10 mm | 2270/6 mm |
| Material | stainless steel | stainless steel |
| Radiation shield (50 K) | | |
| Inner/outer diameter | 5330/5950 mm | 268/800 mm |
| Length/thickness/material | 5370 mm/5 mm/Al | 2135 mm/1.2 mm/Cu |
| Overall weight (rad. length) | 74.5 t for coil (1.2 X ₀) | 6.8 t |
| Operational performance | | |
| Power supply voltage | 12 V | 7 V |
| Current nominal (max.) | 5517 (6000) A | 870 (1000) A |
| Run up (down) time | 80 (120) min | 40 (40) min |
| Cooling time | 168 h | 168 h |
| He flow (4.5/50 K) | 40/3 g s ⁻¹ | 1.3/1.3 g s ⁻¹ |
| Cryogenic losses (4.5/50 K) | 60/420 W | 12.2/34.6 W |
| Total stored energy | 120 MJ | 1.87 MJ |
| Fast discharge time constant | 60 s | 40 ms |
| Fast discharge voltage | 750 V | 860 V |
| Field on axis (integral) | 1.15 T (8.32 Tm) | 4.83 T (8.74 Tm) |

under small angles and for photons from initial state radiation.

4.1. System overview

The luminosity is determined from the rate of Bethe-Heitler events $ep \rightarrow epy$ [24]. The main source of background is bremsstrahlung from the residual gas in the beam pipe, $eA \rightarrow eA\gamma$. At design luminosity these events are expected at 10% of the $ep \rightarrow epy$ rate, but can be subtracted using data from electron pilot bunches. The luminosity is calculated as

$$L = \frac{R_{\text{tot}} - (I_{\text{tot}}/I_0)R_0}{\sigma_{\text{vis}}},$$

where R_{tot} is the total rate of the bremsstrahlung events, R_0 is the rate in the electron pilot bunches, I_{tot} , I_0 are the corresponding electron beam currents and σ_{vis} is the visible

part of the $ep \rightarrow epy$ cross-section with acceptance and trigger efficiency included.

The luminosity monitor detects scattered electrons and outgoing photons in coincidence. It contains therefore two arms: the electron tagger (ET) and the photon detector (PD). Since the angular distributions for both the electrons and photons are strongly peaked in the direction of the primary e-beam – at 30 GeV polar angles are of the order of $\theta \simeq O(m/E) \simeq 17 \mu\text{rad}$ – the detectors have to be placed close to the beamline and from the interaction region in order to cover these small angles.

The general view of the luminosity system is shown in Fig. 9. Scattered electrons are deflected by a set of low-beta quadrupoles and a bending magnet located in the region $5.8 \text{ m} < -z < 23.8 \text{ m}$, pass an exit window at $-z = 27.3 \text{ m}$ and hit the ET at $-z = 33.4 \text{ m}$. The photons leave the proton beam pipe through a window at $-z = 92.3 \text{ m}$, where the beam pipe bends upward, and hit the PD at $-z = 102.9 \text{ m}$. A Pb filter ($2 X_0$) followed by a water Cherenkov ($1 X_0$)

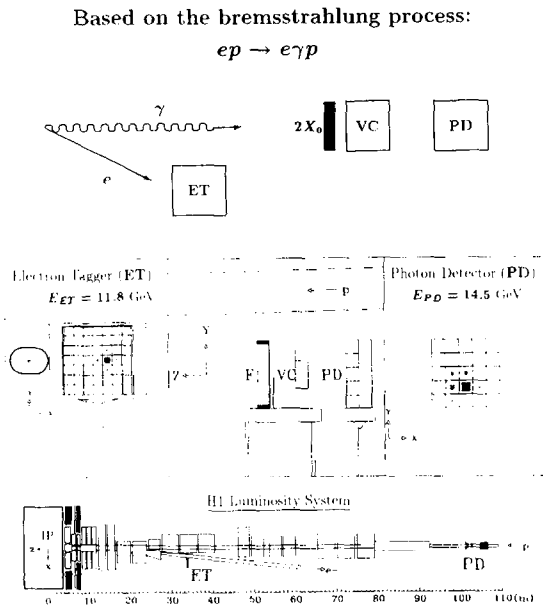


Fig. 9. The layout of the luminosity system.

veto counter (VC) protects the detector from the high synchrotron radiation flux. From the p -beam side the PD is shielded by an iron wall of 2 m thickness. The VC eliminates events with photons interacting in the filter. Both the ET and PD can be remotely moved from the median plane of the e -beam during injection. This operation can be reversed within 1–2 min with a position accuracy of $\sim 100 \mu\text{m}$.

The acceptance of the luminosity system for nominal electron beam conditions ($E_e = 30 \text{ GeV}$, zero tilt) and the expected rates at the design luminosity of $1.5 \times 10^{31} \text{ cm}^{-2} \text{ s}^{-1}$ are given in the Table 3. One of the main contributions to the systematic error in the absolute luminosity measurement comes from the dependence of the system acceptance on possible variations of the electron beam angle in the interaction region. This tilt, typically of the order of $100 \mu\text{rad}$, is controlled by the position of the beam profile at the PD with high precision, of the order of $10 \mu\text{rad}$. The corresponding corrections to σ_{vis} are taken into account already online and can be further improved during the offline analysis.

Quasi-real photoproduction events with $Q^2 < 0.01 \text{ GeV}^2$ can be tagged by the ET in the energy interval $0.2 < E_e'/E_e < 0.8$ using both the PD and VC as a veto.

4.2. Detectors

The design goals – high radiation resistance, good energy, coordinate and time resolution and compactness – were best met by a hodoscope of total absorption KRS-15 crystal Cherenkov counters. Their properties are summarized in Table 3.

Each calorimeter cell is viewed by a FEU-147 photomultiplier [25] with a 20 mm diameter cathode coupled to the crystal with an optical contact. The veto counter is viewed

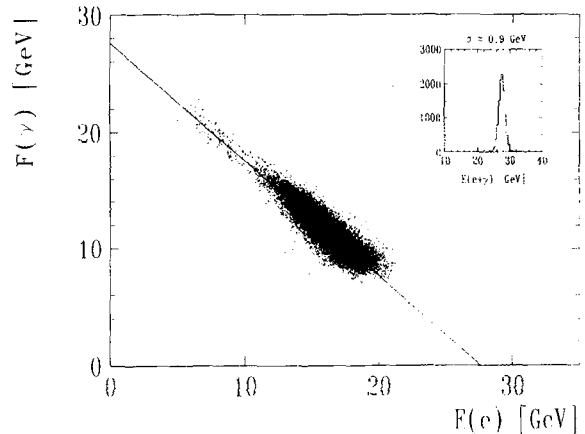


Fig. 10. e - γ energy correlation for bremsstrahlung events detected by the luminosity calorimeters. In the upper right corner the total reconstructed energy is shown. These data are from the beginning of the 1994 HERA e^-p run at $27.5 \text{ GeV} \times 820 \text{ GeV}$ collision energy.

by two phototubes operating in different regimes, the first for photon detection, the second operating with increased voltage and reaching full efficiency for charged particles with a range exceeding 35 cm. Taking into account the material in front of VC, this corresponds to full efficiency for c.m. showers initiated by the photons with $E_\gamma > 1.5 \text{ GeV}$.

Since the luminosity detectors operate at high rates up to few MHz, which may vary within one beam filling by a factor of 3 to 10, they are permanently calibrated during data taking using the energy constraint $E_{\text{ET}} + E_{\text{PD}} = E_{e\text{-beam}}$. Although the calibration coefficients may change within 5–20%, this method allows an absolute calibration with a precision of better than 1%. Fig. 10 illustrates this energy correlation between the two arms.

4.3. Trigger and data acquisition

The different functions of the luminosity system required a special trigger and data acquisition concept, based on the two completely independent branches. The photomultiplier signals pass first differential preamplifiers close to the detectors and then, after 170 m or 100 m of fast coaxial cable pairs, respectively, are again shaped and amplified at the trigger electronics crate. This solution reduces noise and compensates for signal attenuation in the cables. Then the signals are split and analysed in two groups of FADCs (2×80 channels).

The first FADC group operates in a standard mode, similar to all other subdetector trigger systems (see Section 5.3.4). The trigger electronics discriminates the analog energy sums against the individually set thresholds, producing a dead time free trigger bit synchronized to the HERA beam crossing. Three basic trigger signals are available from the electron arm ($E_{\text{ET}} > E_{\text{ET}}^{\text{thr}}$), the photon arm ($E_{\text{PD+VC}} > E_{\text{PD+VC}}^{\text{thr}}$), and the veto counter. The main TE used so far for tagged γp physics was $e\text{TAG} = \text{ET} * \text{PD} * \text{VC}$. The front end readout and the data transfer to the central data acquisition are done by

Table 3

Parameters of the luminosity system ^{a)} at design luminosity and ^{b)} values reached at HERA.

| | Unit | ET | PD |
|---|-----------------|--|---------------------------------|
| Energy interval, $E_\gamma/E_e = 1 - E_{e'}/E_e$ | | 0.2-0.8 | 0.004-1.0 |
| Polar angle acceptance interval | mrad | 0-5 | 0-0.45 |
| Average acceptance for $ep \rightarrow e\gamma$ | % | 48 | 98 |
| Average acceptance for photoproduction | % | 36 | - |
| σ_{vis} | mb | 28 | 174 |
| $ep \rightarrow e\gamma$ rate for $E > E_{thr} = 4 \text{ GeV}$ ^{a)} | MHz | 0.4 | 1.3 |
| Photoproduction event rate ^{a)} | Hz | 20-30 | - |
| Aperture $x \times y$ (granularity) | mm ² | 154 \times 154 (7 \times 7) | 100 \times 100 (5 \times 5) |
| Chemical composition | | TlCl (78%) + TlBr (22%) | |
| Radiation length (Moliere radius) | cm | 0.93 (2.10) | |
| Crystal length (radiation hardness) | cm (rad) | 20 ($> 6 \times 10^7$) | |
| Energy resolution, σ_E/E ^{b)} | % | $1 \oplus 10/\sqrt{E}$, (E in GeV) | |
| Position (time) resolution, $\sigma_{x,y} (\sigma_t)$ ^{b)} | mm (ns) | 0.3-1.2 (<3) | |

a program running on the FIC8230 master processor [26].

The second FADC group is controlled locally and completely decoupled from the H1 trigger system. Two triggers are used for the luminosity calculation and online detector calibration: $ET \cdot PD$ and $ET \cdot PD \cdot \sqrt{VC}$. Any combination of 5 TEs can be permanently stored without dead time for each of the 220 bunches in a fast histogramming memory of 32×220 channels. This memory contains the full information on all bunch related trigger statistics, e.g. the level of accidental coincidences. The online event processing includes fast reconstruction, calibration, trigger verification and calculation of the current luminosity and is performed on a second FIC8230 processor.

4.4. Performance

The system has been working successfully since April 1992. A typical example of the information provided by the luminosity system during e-p collisions is shown in Fig. 11. For safety reasons lead-scintillator calorimeters were used in 1991 [27] during the running in phase of HERA. In the early phase, when HERA operated at 1% of the design luminosity, the detectors were active even during injection and ramping of the electron beam, which allowed the machine crew to better understand the beam dynamics and to adjust for collisions quickly.

The total integrated luminosity measured in 1993 and 1994 by H1 is shown in Fig. 6. The present understanding of the systematic error is summarized in the Table 4. Due to the redundancy in the trigger, the systematic error can be further reduced by combining the present method with other possible triggers (e.g. with the total photon flux measurements [28] etc.). The data sample taken with the help of the eTAG trigger of the luminosity system was the starting point for all photoproduction results presented by H1 so far [29,30].

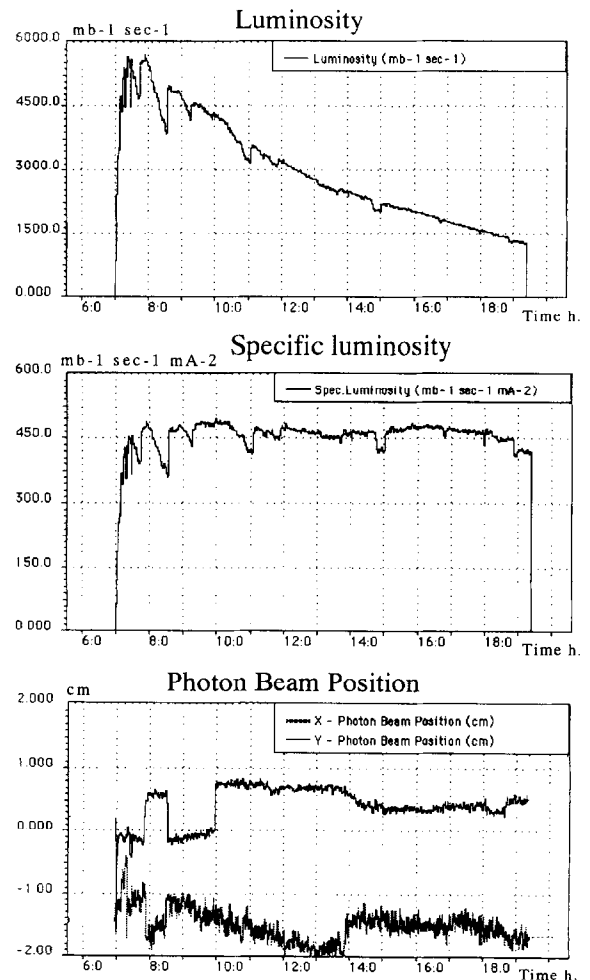


Fig. 11. Data provided by the luminosity system during the e-p collisions at HERA. Statistical fluctuations correspond to one measurement every 10 s.

Table 4
Systematic error for the absolute luminosity measurement. (Based on the offline γ -rate method)

| Contribution to $\delta\mathcal{L}$ | 1993 | | | |
|--|------------------|------------------|------------------|------------|
| | e ⁻ p | e ⁻ p | e ⁺ p | shifted IP |
| 1. Theoretical value for σ_{BH} | 0.5% | | 0.5% | |
| 2. Trigger efficiency | 2.0% | | 0.3% | |
| 3. Statistics, e-gas bgrd. subtraction | 1.5% | 1.3% | 0.4% | 3.3% |
| 4. γ -energy scale (calib & resol.) | 1.7% | 1.1% | 0.9% | 1.7% |
| 5. Geometrical acceptance of γ -arm | 0.7% | | 0.5% | |
| 6. Multiple photon effect (pileup) | 0.2% | 0.3% | 0.4% | 0.3% |
| 7. Counting and rounding errors | 1.1% | | 0.5% | |
| Total error from lumi system | 3.4% | 2.0% | 1.4% | 3.8% |

5. Trigger

5.1. Introduction and trigger requirements

The task of the trigger system is to select out of the flow of signals registered in the multitude of detector channels those for permanent recording that originate from a given e-p interaction of physics interest and to reject background events. The common background sources of other accelerator experiments are also present at HERA: synchrotron radiation from the electron beam, proton gas interaction in the beam pipe vacuum of about 10^{-9} hPa and stray protons, which produce particle showers by hitting the beam tube and other materials around the accelerator. Beam halo muons and muons from cosmic radiation play a rôle, too.

The variety of physics processes under study in e-p collisions covers a wide range of cross-sections and of rates, respectively. It extends from photoproduction, where the visible e-p cross section of several μb implies an event rate of 20–30 Hz at design luminosity ($\mathcal{L} = 1.5 \times 10^{31} \text{ cm}^2\text{s}^{-1}$), towards W production expected to occur a few times per week. (See Table 5.)

The high luminosity mandatory for the measurement of the rare processes could only be achieved with a large number of proton and electron bunches in the machine (see Section 2.4). With a basic proton RF frequency of 52 MHz (208 MHz) 210 bunch positions have been foreseen along the circumference of the storage ring; consequently the

Table 5
Cross sections and rates (at design luminosity).

| | | |
|--|-------------------|-----------------------|
| Beam gas interactions | | 50 kHz |
| Cosmic μ in barrel | | 700 Hz |
| Tagged γp | 1.6 μb | 25 Hz |
| c $\bar{\text{c}}$ total | 1 μb | 15 Hz |
| DIS low Q^2 | 150 nb | 2.2 Hz |
| DIS high Q^2 (e in LAr) | 1.5 nb | 1.4 min^{-1} |
| Charged current DIS $p_T > 25 \text{ GeV}$ | 50 pb | 3.0 h^{-1} |
| W production | 0.4 pb | 0.5 d^{-1} |

Table 6
Time scales at HERA and H1.

| | |
|--------------------------------------|------------------------|
| Width of proton bunch | 1.4 ns |
| Distance to next satellite bunch | 5 ns |
| Flight time to backward ToF | 6 ns |
| Flight time to barrel muon system | 20 ns |
| Bunch crossing interval | 96 ns |
| Longest drift time in CJC | 1 μs |
| Integration time of LAr preamplifier | 1.5 μs |
| Delay of first level trigger | 2.5 μs |
| Front end readout time | $\approx 1 \text{ ms}$ |

bunch crossing interval is 96 ns.

This time span has to be compared to typical signal formation times in the detector: the largest drift times in the central jet chamber (CJC) amount to 1 μs and the calorimeter preamplifier has an integration time of about 1.5 μs . (see Table 6.)

The probabilities per bunch crossing for accidental tracks, calorimeter energy deposits or electron tagger signals are at or below the percent level. However, when integrated over the detector sampling times, the pile-up probability is no longer negligible. Therefore it is mandatory that the trigger identifies the bunch crossing (“ t_0 ”) associated to the event under consideration.

Most subdetectors of H1 generate signals that can be used for the first level trigger. Some examples are: tracks in certain ranges of curvature, energy depositions with their topology, interaction vertex positions, particle arrival times. Local coincidences between MWPC “rays” and calorimeter “towers” are also formed. While fast detectors like MWPCs and scintillators intrinsically provide time resolution within a bunch crossing, “ t_0 ” information can be obtained from calorimeter signals using constant fraction methods, or from the drift chambers by requiring special track configurations. In contrast, threshold-like signals extend over several bunch crossings and have to be put into coincidence with external “ t_0 ” bits.

The first level trigger thus provides a decision for each bunch crossing. The fully pipelined system runs deadtime free at 10.4 MHz and is phase locked to the RF signal of HERA. The decision delay of 2.5 μs determines the minimum pipeline length needed to store the full detector data at the front end.

The asymmetric beam energies of HERA give rise to strongly forward-directed event topologies that are hard to discriminate against background from proton interactions with residual gas atoms. Already at first level, the trigger system has to provide a sophisticated identification of the characteristics of an event and to trigger on the complex signatures of physics processes. To this end, the trigger subsystems of H1 deliver information on distinct properties of the event. In several different ways, use is made on the track origin information that uniquely distinguishes e-p interactions from the beam gas background. Early arrival times in the ToF system indicate that the origin of the event is upstream

the proton beam. A large distance of closest approach to the beam axis of CJC measured tracks in the (x, y) plane, or along the beam axis (from the z drift chambers) distinguishes events not produced in the fiducial volume of the interaction region. In addition, a fast estimate of the z vertex position along the beam axis based on histogramming techniques of signals from the central and forward proportional chambers, constrains the vertex even further.

For some $e-p$ events the vertex information may not be the best requirement at the first trigger level. The signature of the scattered electron can be exploited where appropriate. Depending on the Q^2 region under consideration, it is detected in the electron tagger of the luminosity system, in the backward electromagnetic or in the main LAr calorimeter. Next, the topology of the hadronic final state is widely used. Charge current (CC) events are identified by the imbalance of transverse component of the hadronic energy deposition. Jet signatures spot hard photoproduction events, and the requirement of a positive muon signal serves as a tag for heavy quark production. It has even been possible to trigger on heavy quark production events without detection of the scattered electron, relying just on the topology of the registered charged tracks.

An obvious possible extension of the system is to make use of local correlations between the trigger “objects” of different subsystems. “Some track” together with “some muon signal” is more likely being randomly produced than a “track pointing to a muon signal” in space. Probabilities for accidental coincidences are reduced with increasing granularity.

While at first trigger level only the MWPC and LAr calorimeter data are correlated in such a way, full use of the detailed, high granularity trigger data of most subsystems is being made in the intermediate trigger levels 2 and 3. With decision times of 20 μs and 800 μs , respectively, they work within the primary dead time. The level 2 decision is made using purpose built hardware. A KEEP decision at level 2 initiates the readout of the front end under processor control. In parallel, a flexible level 3 system with software algorithms running on a RISC microprocessor can refine the trigger and potentially abort the readout.

5.2. Front end pipelining

The time interval between two consecutive bunch crossings of 96 ns is used as the time unit (1 BC) in the following. The time needed to run trigger signals even through a few electronics circuits performing simple logical calculations is usually longer than that. Moreover the large size of the experiment introduces cable delays of several BC. Finally certain subdetectors have a long detector response time which means that the information of these detectors is only available some BC after the event (LAr: 13 BC due to long integration time of the preamplifiers, central drift chamber: 11 BC due to a longest drift time of 1 μs). Such long response times can only be tolerated because, due to the relatively low event rate (compared to a $p-p$ collider),

the probability for an $e-p$ interaction per bunch crossing is small (of order 10^{-3}).

The L1 trigger decision (called L1keep signal) is available centrally 24 BC after the real $e-p$ interaction. Further time is needed to distribute this signal to stop the various subdetector pipelines, otherwise the information which belongs to the relevant BC would be lost. The pipeline length varies between 27 and 35 BC depending on the subdetector, which is just long enough to operate the system. For future system designs we would advise to increase this pipeline length to gain more flexibility in the timing of such a system or - even better - to perform signal processing and zero suppression before entering the pipelines and store the information dynamically.

This concept of a pipelined front end system also avoids a huge amount of analog cable delays and allows to reconstruct offline the history of the event over several BC for timing studies and to identify signal pile up.

H1 uses four different types of pipelines (For a more detailed description of the electronics see the Sections of the respective detectors):

- Fast random access memory (RAM) is used to store the digitized information of the drift chambers (central and forward tracker, forward muon system) as well as of the LAr calorimeter for trigger purposes. The analog to digital converters operate at a frequency of 10.4 MHz for the LAr calorimeter and 104 MHz for the drift chambers. They are synchronized to the HERA clock which is also used to increment the 8-bit address of the RAM, operating as a circular buffer. At L1keep time writing into the RAMs is disabled to save the information for the readout process. In addition RAM buffers are used to pipeline information in the drift chamber trigger and in the central trigger.
- Digital shift registers are used to store the single bit information, generated by threshold discriminators followed by a special HERA clock phase synchronization circuit, in the instrumented iron system, the multiwire proportional chambers, the drift chamber trigger branch, the BEMC trigger branch and the ToF and Veto wall scintillator systems. A custom designed gate array contains the clock synchronization circuit and a 8 channel 32 stage pipeline realized as D-Flip-flops. See the Section 4.1.4 of Ref. [9] for a description of this gate array.
- Analog delay lines are used to store the pulse height of the BEMC. The L1keep signal is used to stop a sample and hold circuit from which the digitization takes place during the dead time of the readout.
- Signal pulse-shaping of the LAr and TC is adjusted such, that the signal's maximum occurs at L1keep time. The same type of sample and hold and digitization is used as in the BEMC case.

The timing of the synchronization step and the analog to digital conversion clocks is critical. The information has to be uniquely attributed to the BC the event originated from. The adjustment of the HERA clock phase, which defines this synchronization time in each subsystem, is therefore a

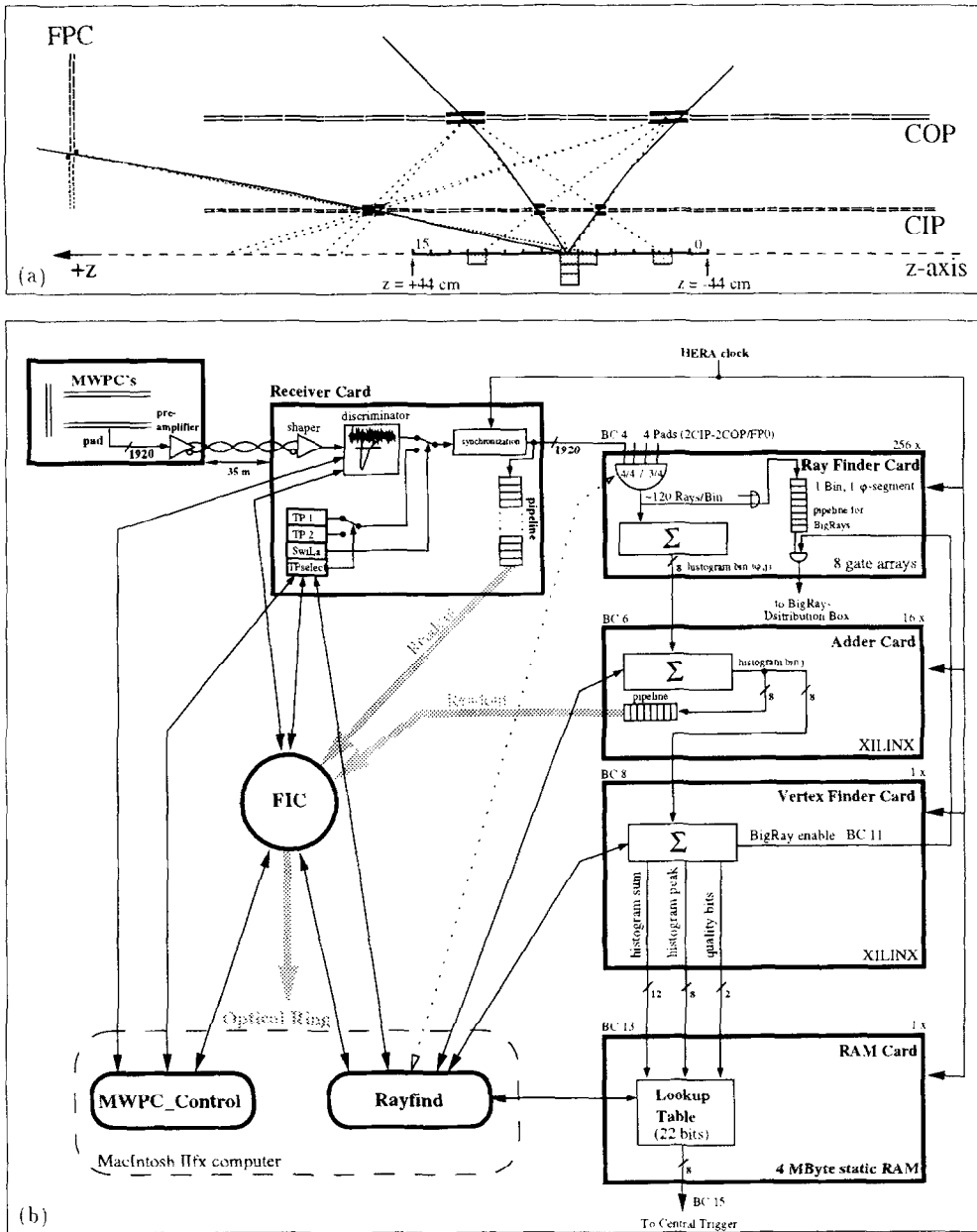


Fig. 12. (a) z -vertex reconstruction by building a histogram, which displays a peak at the true vertex location. (b) Block diagram of the z -vertex trigger.

major task, which required several iterations of delay curves combined with offline analysis, and it turned out to be a much more complex operation than expected. Online bunch and clock phase monitors ensure stable operation at the correct timing values.

5.3. Trigger level 1

The trigger level 1 system [31] consists of nine different trigger systems each based on the information of a subdetector. The outputs of these systems are called trigger elements

(TE). These TE are fed to the CTL where they are combined to various so-called subtriggers. Each single subtrigger suffices to produce a L1 keep signal to stop the pipelines and initiate the event readout.

In the following paragraphs the nine systems and the CTL are described.

5.3.1. Vertex position oriented trigger systems

The geometrical origin of the event is the main handle to suppress background at a HERA experiment. Vertices which lie outside the nominal e-p interaction region identify

uniquely background events. These TE are therefore in one or the other way used for almost all subtriggers, with the exception of the higher threshold triggers of the calorimeters.

The backward time-of-flight system Beam-wall and beam-gas events originating from the proton beam produce showers, which mostly penetrate both scintillator walls (see Section 2.7 of Ref. [9]) behind the BEMC. A background (BG) and an interaction (IA) timing window (derived from the HERA clock signal) define for each scintillator whether the hits belong to particles arriving directly from upstream or via the longer path from the nominal interaction region. The signals from the single scintillator sheets of each wall are logically “ORed” together to form a signal for each plane, and the two planes are then put into coincidence forming the trigger elements ToF-BG and ToF-IA.

The ToF-BG signal is the simplest and most effective background rejection criterium and is therefore applied to most of the physics subtriggers as a veto condition. The logic is realized in conventional NIM electronics.

The z -vertex trigger The central and the first forward proportional chamber are used to estimate the event vertex position along the beam axis (z -axis) (for a more detailed description see Ref. [32]). A particle originating from the beam passes four layers of chambers (either the double layers of CIP and COP or CIP and first forward proportional chamber). The first step of the vertex estimator, the so-called rayfinder, therefore combines the four cathode pad signals (see Section 2.5.2 of Ref. [9]) which lie on a straight line into an object called ray. In the plane perpendicular to the beam a 16 fold segmentation (ϕ -sectors) is used, such that the rays of each segment are treated separately. A total of 34'400 different rays are examined for each bunch crossing simultaneously.

A histogram with 16 bins along z with a bin width of 5.4 cm is filled according to the z -coordinate of the origin of each ray. The rays formed by the correct combinations of pads all enter in the same bin and consequently form a significant peak above the background generated by rays from wrong combinations of pads which are more or less randomly distributed (see Fig. 12(a)). Events which have their vertex far outside from the nominal interaction region do not develop significant peaks, in this case the histogram contains only the background from accidentally formed rays.

From this histogram various TE are derived. The $zVTX-t0$ TE is activated if there is at least one entry in the histogram. $zVTX-t0$ indicates a minimum of activity in the central region of H1 and also serves for bunch crossing identification in combination with low threshold energy triggers of the calorimeters. The two TE $zVTX-sig1$ or $zVTX-sig2$ are activated if the histogram peak exceeds a given significance threshold (two different threshold settings are available in parallel). For events with a few tracks only, a special TE indicates that there were only few entries in the histogram albeit in a single cluster. The histogram analysis is fully pro-

grammable, such that the meaning of the TE can easily be changed.

The rayfinder is based on a custom designed gate array (1.5 μm CMOS technology), of which 2112 pieces are in use. It contains the logic to examine the signals of 45 cathode pads and to form 30 rays (allowing a flexible 3 out of 4 logic), the adder tree to count the active rays, the grouping of these rays into big rays (see below) and some pipeline structure for delays. For the final histogram building and the peak analysis programmable logic cell arrays (XILINX family 3000 [33]) and a 22 bit look up table realized with 4 MByte of fast static RAM are used (see Fig. 12(b) for a block diagram).

The forward ray trigger The cathode pad signals of the FPC and the CIP are fed into a logic circuit which finds rays originating from the nominal interaction region and pointing in the forward direction (for more detailed description see Ref. [34]). A ray here is a set of impacts on three or four chambers, compatible with a track coming from the interaction region in one $2\pi/16$ ϕ -sector. Out of the 6 or 8 chamber planes (2 planes per chamber) which are hit by the track, only one is allowed to be absent. For each of the 16 ϕ -sectors there are 32 possible rays corresponding to radial bands for impacts on the second FPC. The width of these bands increases in geometrical progression, the lowest radius is 21 cm, and the largest one 75 cm, corresponding to angles of 5.63° and 24.72° respectively.

These rays are counted and a TE is activated if at least one road is found. Other TE indicate active rays in adjacent ϕ -sectors (the xy plane is divided into 16 ϕ -sectors as in the z -vertex trigger above). Furthermore, special topology conditions in the 16 ϕ -sectors can be used to activate a TE, e.g. a back to back of all rays.

This system is realized by a total of 320 RAMs, which are used as hierarchically organized look up tables.

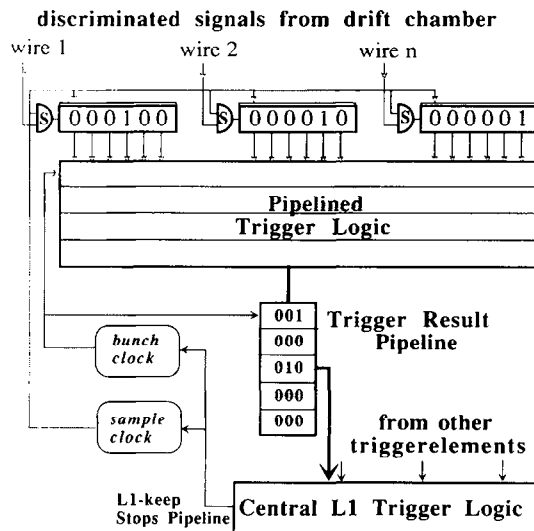


Fig. 13. Block diagram of the drift chamber trigger.

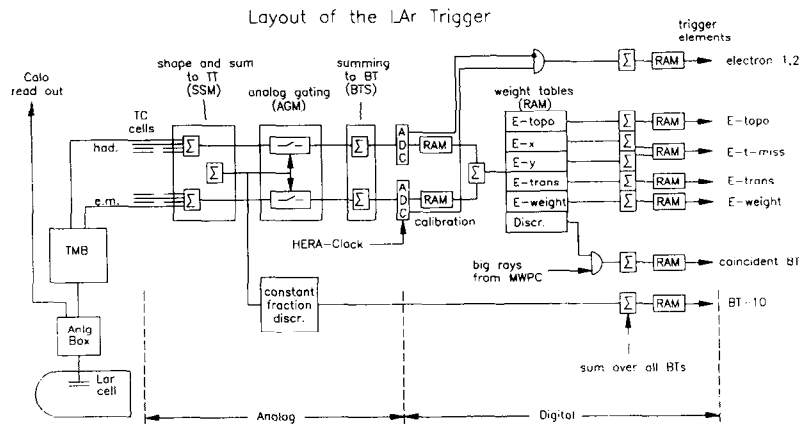


Fig. 14. Block diagram of the liquid argon calorimeter trigger.

Other MWPC triggers Additional TE are derived from the CIP to trigger on cosmic rays passing through the beam pipe.

If more than three sectors in the backward quarter of the CIP are set, the TE CIP-backward might indicate an upstream p beam-gas event. The TE is used as a veto for certain subtriggers which are derived from tracking information only.

Big rays The rays found by the forward ray trigger and the z -vertex trigger (in the latter case only the rays originating from the highest peak in the z -vertex histogram, Fig. 12(b)) are extrapolated and combined to 224 "regions of interest" so-called "big rays", which have the same geometrical division as the "big towers" of the liquid argon calorimeter trigger (see below and Fig. 15). They "rays" can both be put into coincidence with the "towers" (Fig. 14) but also be used in a stand alone manner by demanding topological conditions (e.g. back-to-back configuration or minimal multiplicity in backward region) on the pattern of MWPC rays.

The central jet chamber trigger This trigger [35] finds tracks in the CJC, which have a distance of closest approach to the nominal beam line of less than 2 cm from the nominal beam axis and therefore suppresses beam-wall events as well as synchrotron radiation background. To keep the number of channels at a manageable level without degrading the performance 10 selected layers out of 56 radial signal wire layers of the CJC are used in the trigger.

In a first step (Fig. 13) the signals from the CJC are digitized by a threshold comparator (independent of the normal readout branch) and synchronized to the HERA clock. This way the drift time information is kept with an accuracy of 96 ns corresponding to about 5 mm of position resolution. For the innermost two drift cells this resolution is improved by doubling the clock frequency.

In a second stage the hits are serially clocked into shift registers. Hit masks are defined according to track position in drift space and track curvature in the magnetic field. A total of 10000 different masks are applied in parallel to the

outputs of the shift registers to mark the active roads. Tracks with low or high transverse momentum can be distinguished as well as the charge of low momentum tracks ($< 1 \text{ GeV}/c$). The number of roads found in each of the 15 ϕ -segments and in the two momentum bins for each charge are counted separately in 3 bit numbers.

In the final step these track counts are processed to generate the TE. Three different thresholds on the total number of tracks are implemented. In addition a topological analysis in the xy plane is performed, for instance back to back tracks in ϕ can be recognized.

Most of the digital logic is programmed into about 1200 programmable logic cell arrays (XILINX [33] family 3000).

The z -chamber trigger The z -chamber trigger [36] uses the signals of the drift chambers CIZ and COZ in a way similar to the central $r\phi$ jet chamber trigger, utilizing the relatively high spatial resolution obtained from the drift chambers. Signals are synchronized with twice the HERA bunch frequency and stored in shift register pipelines. Their parallel outputs are fed into coincidence circuits used as look up tables for all possible tracks coming either out of the interaction region of 50 cm length (vertex tracks), or from the upstream proton beam region with $20^\circ \leq \theta \leq 90^\circ$ with respect to the beam line (background tracks).

In a first step tracks are found with a granularity of 2.4 mm within the individual CIZ and COZ systems. For tracks originating from the vertex signals from CIZ and COZ are combined in a 96 bin vertex histogram using an analog technique. By gating the system with an OR of the central proportional chambers the search for a peak in this histogram can optionally be further restricted. A resolution of 5 mm for the vertex reconstruction is achieved. The drift cells associated with a vertex track (both left and right solutions in drift space) are stored thus providing a fast θ measurement of a track.

Tracks not associated with the fiducial volume of the interaction region are counted as upstream background, a sig-

nal that can be used as an effective veto.

The shift registers and the look up tables are configured in 1060 logic cell arrays (XILINX [33] family 3064 and 3090).

5.3.2. Calorimetric triggers

The selection of deep inelastic e–p reactions is based primarily on calorimetric triggers. These events are characterized by large transverse energy depositions originating from jets and eventually the primary scattered electron. Certain physics channels “beyond the standard model” are expected to lead to similar event signatures. Correspondingly, the calorimeter triggers have to cope with a wide spectrum of trigger observables, from narrow, localized energy depositions (e.g. electrons) to global energy sums such as transverse or missing transverse energy. Even photoproduction events with heavy quarks, with energy deposits as small as 1–2 GeV, should be efficiently detected, when the calorimeter signal is locally put into coincidence with big rays from the MWPC system.

The liquid argon calorimeter trigger The liquid argon trigger [37] system is designed to calculate the energy deposited in various parts of the calorimeter as well as the total energy and other global energy sums which can be weighted by position-dependent weighting factors.

The realization of this system contains an analog and a digital part (Fig. 14). In the analog part the signals from the calorimeter cells are split off the readout chain after the preamplifier and are separately amplified and shaped to a pulse width of about 600 ns FWHM. Signals within a Trigger Tower (TT) are summed. The TTs are approximately pointing to the vertex and are segmented in 23 bins in θ and in 32 bins or less in ϕ . While the electromagnetic and hadronic signals are still separated in the TTs, the sum of the two is fed into an analog discriminator which turns both signals off for later summing, if the level is below an adjustable threshold (“AGM threshold”) as determined by the electronic noise. The same signal is used to determine the time of the signal (t_0) by a constant fraction type method. The boolean number of $t_0 > 0$ is available as a TE (LAr-T0). Using the trigger for low threshold photoproduction physics requires a precise adjustment of thresholds already at the analog stage. This is possible by cross calibrating the trigger to the more precise ADC readout [38].

Depending on the θ region, either one, two or four TTs are summed up to “big towers” (BT), providing finer granularity in the forward direction (Fig. 15). A total of 240 such BT’s are formed from the ≈ 45000 LAr cells, another 12 BT’s are derived in a similar way from the signals of the BEMC and the PLUG calorimeter.

The electromagnetic and hadronic signals of each BT are digitized separately by analog to digital converters running at the HERA clock frequency of 10.4 MHz. The digital outputs are calibrated by a RAM look up table and two threshold discriminators are used to look in each BT for a poten-

tial electron signature defined by high electromagnetic and low hadronic energy in the respective sections of the tower. Another discriminator look up table marks all BT’s to be transferred to the higher trigger levels. The electromagnetic and hadronic parts of each BT are summed and the total BT energies are then available for further processing. A threshold is set on the total BT signal in coincidence with the “big rays” as derived from the MWPC triggers (see Section 5.3.1). The number of these towers is counted, discriminated and provided as a trigger element to the CTL.

The total BT energy is fed into a set of look up tables producing the weighted energy of this big tower for the global sums: For the total transverse energy a weight of $\sin \theta$ is used, the transverse components E_x and E_y are obtained by multiplication with $\sin \theta \cos \phi$ and $\sin \theta \sin \phi$, respectively, to build the missing energy signal. A further channel can be used for arbitrary purposes, e.g. for generating a trigger with uniformly distributed rates over the polar angle by weighting each BT with the inverse of the background rate of its angular region. A “topological” channel allows to sum up separately the energies in five predefined topological regions (BEMC, central barrel (CB), forward barrel (FB), inner forward (IF), and PLUG). For these regions, the total energy as well as the energies in each of the contributing quadrants are calculated. Furthermore the total energies are calculated for the total barrel (CB+FB) and the forward (IF+PLUG) and backward (FB+CB+BEMC) regions. For the summing of the weighted BT energies, custom specific gate arrays are used with 8 bit accuracy (7 bit plus sign for E_x , E_y).

In the last step further RAM-based look up tables are used to encode the various global and topological sums into two-bit threshold functions provided as TE to the CTL. One such look up table also builds the missing energy from the two signed components E_x and E_y with subsequent discrimination and encoding into two bits.

More details about this trigger and its performance in 1994 can be found in Ref. [39].

The BEMC single electron trigger The purpose of the BEMC Single Electron Trigger (BSET) (see Refs. [40,41]) is to identify scattered electrons from DIS processes in the angular acceptance of the BEMC. The basic concept of this trigger is to provide cluster recognition and to place energy thresholds on the sum of all energy clusters in the BEMC. The trigger is based on energies deposited in BEMC stacks which have a granularity well matched to the transverse spread of electromagnetic showers.

Analog signals from preamplifiers of single wavelength shifters are first added to form stack sums representing a high granularity TE. The summed analog stack signals are then adjusted in their gain and timing in order to provide an equal analog response to energy and to uniquely assign the energy depositions in all stacks to a single HERA bunch crossing. Two thresholds are applied to these signals. A low threshold just above noise level and a medium threshold to be used as a cluster seed. Typical values are 1.3 GeV for the

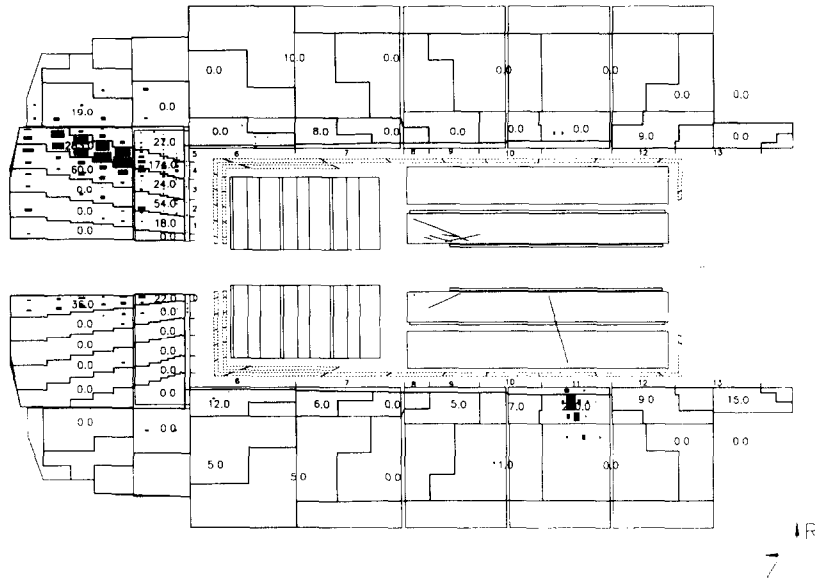


Fig. 15. Cross section through the θ plane of the liquid argon calorimeter showing the pointing geometry of the trigger big towers.

low threshold and 2.3 GeV for the medium one. A cluster identification module then detects the cluster seeds and assigns neighbouring stacks to define clusters. Two TE reflect the cluster multiplicity (one or more clusters, exactly one cluster). The energy of all clusters is summed up and three possible thresholds (CL1, CL2 and CL3) can be placed on this sum, which activate the respective TE. The total energy summed over all stacks exceeding the low threshold is also compared to a threshold and activates another trigger element. Finally the cluster energy and the total energy sum is digitized into an eight-bit number to be used for correlations with other quantities at the CTL.

The trigger has been able to operate in coincidence with a timing veto from the time-of-flight system (see Section 5.3.1) and a cluster threshold of 2.5 GeV during the first data taking period. The threshold curve for the cluster energy is shown in Fig. 16.

5.3.3. Muon triggers

Both the instrumented iron system and the forward muon spectrometer deliver level 1 trigger information, as described below.

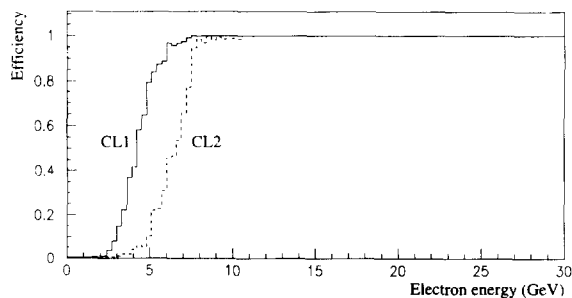


Fig. 16. BEMC single electron trigger efficiency for thresholds CL1 and CL2.

The instrumented iron muon trigger The instrumented iron system is logically divided into 4 subdetectors (front end cap, forward barrel, backward barrel and backward end-cap) [42]. Each subdetector consists of 16 modules. The wire signals of layer numbers 3, 4, 5, 8 and 12 of each module are used for the level 1 trigger. The pipeline gate arrays used in this system have this output available after the synchronization step, but before the entry into the pipeline. The "OR" of 16 wires of these signals is called an element and all elements of one chamber are again ORed together to form a single layer signal. Any condition on the 5 trigger layer signals of one module can be requested by means of RAM look up tables (e.g. 3 out of all 5) for each module independently. Two signal lines per module are used. One of these contains the system's t_0 information, the second is used for the coincidence condition. The latter is transferred to the level 1 trigger after its timing has been set correctly by means of the t_0 signal from the first hit trigger layer in the module. This determines the correct BC with a resolution of about 20ns. On level 1 only 8 TE are left distinguishing between exactly one or more than one module trigger in different regions of the polar angle. The 64 coincidence bits as well as additional information on the multiplicity per module is then ready for use in the level 2 and level 3 trigger systems.

The instrumented iron muon trigger has been used up to now for two main purposes: in combination with other H1 triggers (especially from the tracking system) to trigger on muons from heavy quark decays or from $\gamma\gamma$ interactions or as stand alone trigger for monitoring: either on cosmic muons or on muons in the proton beam halo.

The forward muon trigger The signals from the drift chambers of the forward muon spectrometer are discriminated

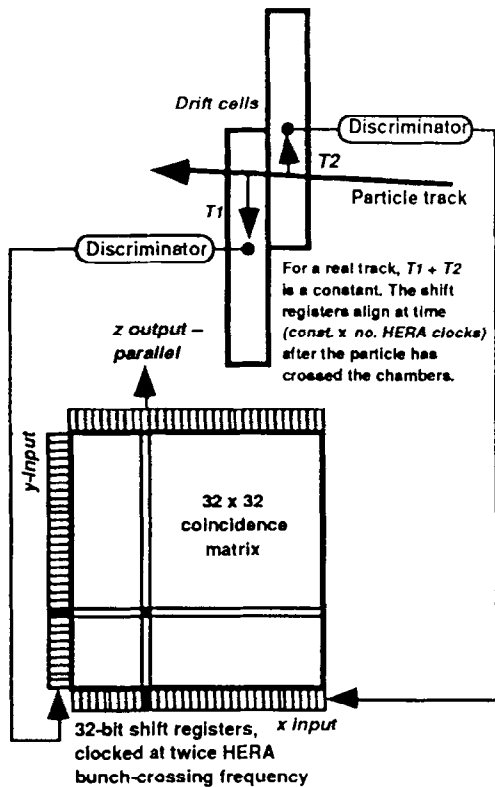


Fig. 17. Principle of track recognition in the forward muon trigger.

and fed into an electronic system which extracts the appropriate t_0 and the coordinate within the drift space of chamber hits which correspond to tracks [43]). This is achieved by making use of the staggered arrangement of two adjacent drift cells as shown in Fig. 17. For correct t_0 the sum of the drift times of the two cells is defined for any track coming from the collision point, while the difference of the two drift times gives the coordinate within the drift space. A field-programmable 32×32 coincidence array with serial-load shift register axes, built in a $1.5 \mu\text{m}$ CMOS custom specific chip is used to make the correlations between the two drift times and thus identify bunch number and track position.

A similar coincidence matrix with parallel-loaded axis is then used to define pairs of track segments which correspond to tracks in the chambers before the toroid and separately in the chambers after the toroid. A variable width road may be applied to require that the tracks point to the interaction vertex. In the third step of this trigger processor pre-toroid and post-toroid tracks are fed into a further coincidence matrix which finds pairs of tracks which have traversed the toroid. The momentum selection of the trigger is made by varying the widths of the roads.

The trigger deals with each octant of the forward muon chambers separately. The track candidates found in each octant are allocated to eight regions at different polar angles relative to the beam. The 8-bit hit patterns from all eight octants are fed into a RAM based look up table which counts the number of muon candidates and allows programmable

topological correlations to be made. Eight bits of trigger information are then sent to the CTL as TE.

5.3.4. Triggers derived from the luminosity system

The luminosity system runs with an independent data acquisition and triggering system as described previously in Section 4.3. However the trigger signals derived from the three detectors of this system are available also to the main trigger system: independent thresholds can be set on the electron energy, the photon energy and the calibrated sum of both. Together with the signals of the veto counter located in front of the photon detector this information is fed into a look up table to form logical combinations. The outputs are connected to the CTL as TE.

So far mainly the electron signal was used to tag photo-production events.

5.3.5. Central trigger level 1 decision

The information generated by the subdetector trigger systems described above consists of 16 groups of 8 TE, which are connected to the CTL inputs [31,44]. The 16 groups of TE are fed into pipelines realized as dual ported RAM based circular buffers, which allows to adjust the delays of all incoming signals to the proper BC. In addition the RAMs can be used to study the time evolution before and after the actual event.

The TE are logically combined to generate a level 1 trigger signal. Up to 128 different subtriggers are formed by applying coincidence and threshold requirements. (Lookup tables are used to form 16 fold coincidences of arbitrary logic expressions from up to 11 predefined input bits). A compact trigger description language (TDL) has been developed to keep up with the ever changing demands for new subtriggers and to properly log the logic and the status of the triggers loaded.

The subtriggers are assigned to a given physics event class (physics trigger), to experimental data needed e.g. for measuring the efficiency of a given detector (monitor trigger) or to cosmic ray events for calibration purposes (cosmics trigger).

The possibility to gate the logic with beam information is also useful; cosmic or calibration triggers should only fire when both bunches are empty, physics triggers only, when both are filled.

The rate of each subtrigger is counted separately and can be prescaled if needed. The final L1keep signal is defined by the logical OR of all subtriggers after prescaling and is distributed to the front end electronics of all subsystems to stop the pipelines. Only at this point the primary dead time starts to accumulate.

5.4. Intermediate trigger levels

The two intermediate trigger levels 2 and 3 operate during primary dead time of the readout and are therefore called synchronous. The calculations which are performed in these

systems and the decision criteria applied depend on the sub-trigger derived in the level 1 system, which acts in this way as a rough event classification.

During the level 2 latency time (a fixed time of typically 20 μs) the level 2 trigger system evaluates a larger number of detector signal correlations typically in a mixed serial/parallel manner. Depending on the outcome of the analysis a fast KEEP or REJECT signal is issued at decision time. For the level 2 decision various hardware solutions are under construction including a complex topological correlator [45] and a neural network approach to exploit the correlations between the trigger quantities from the various subsystems in a multidimensional space [46]. The massively parallel decision algorithm of these systems makes them ideally suited for fast trigger applications.

Only if the event is accepted at level 2, the time consuming readout tasks such as zero-suppressing of the drift chamber digital signals and the calorimeter analog to digital conversion and DSP processing are initiated. During this time the trigger level 3 system based on a AM 29000 RISC processor performs further calculations [47]. The level 3 decision is available after typically a few hundred μs , in case of a reject the readout operations are aborted and the experiment is alive again after a few μs .

The calculations of both level 2 and level 3 triggers are based on the same information prepared by the trigger level 1 systems described in the previous Section: MWPC (Big Rays, z -vertex histogram), central drift chamber (number of tracks found in each ϕ -sector by the level 1 trigger), BEMC (individual stack information, energy sums built in the trigger level 1 system), LAr calorimeter (individual big tower electromagnetic and hadronic energies and the global sums, as built in the trigger level 1 system) and intermediate information generated by the main and forward muon triggers. Topological and other complex correlations between these values are the main applications for the intermediate trigger systems.

The events which survive the level 2 and 3 triggers are taken over by the central data acquisition system with a typical maximum rate of 50 Hz (see Section 7 for upgrading state of this limit). Since this system works asynchronous to the primary trigger system, there is no further dead time involved as long as the level 3 accept rate stays safely below these 50 Hz. The decision times of these systems (level 2: 20 μs , level 3: assume 100 μs average) and the total primary dead time of about 1.5 ms for fully accepted events imply, that the level 1 (level 2) trigger accept rate must not exceed 1000 Hz (200Hz) to be able to run the experiment with an overall dead time below 10%.

Fig. 18 indicates the front end response time as a function of the instantaneous input rate. The time is independent of the “distance” between two events until at high input rates 2nd order limitations come into play. One such effect has been identified in the drift chamber readout and been cured by introducing deeper buffering at the front end.

At present the level 2 and 3 processing systems have not

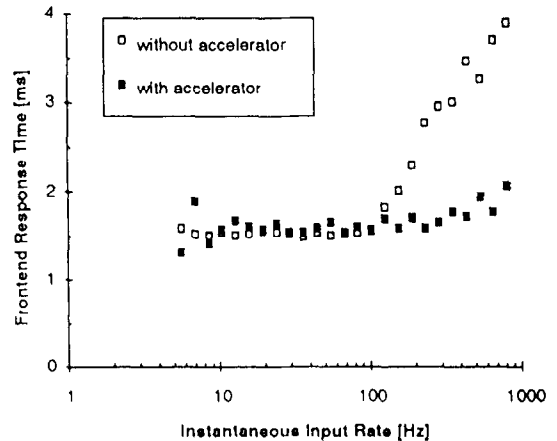


Fig. 18. The frontend response time as a function of the instantaneous input frequency ($= 1/\text{time between consecutive events}$). The increase at rates above 100 Hz is related to a buffering limitation in the drift chamber readout, which has subsequently been cured.

yet been in use. (However, all accept and reject control signals were available and the system can be run by arbitrarily forcing level 2 and level 3 accept/reject decisions for each event.) The level 1 accept rate had therefore to meet the central data acquisition limitation of 50 Hz. Since the “physics content” of the TE information is already appreciable this can typically be done in a straight forward manner. Special caution, however, is appropriate when the background conditions of the beams change dramatically, which may happen from time to time.

5.5. The level 4 filter farm

The level 4 filter farm is an asynchronous software trigger based on fast MIPS R3000 based processor boards [48]. It is integrated into the central data acquisition system and has the raw data of the full event available as a basis for its decision making algorithms. This allows for online trigger selections with the full intrinsic detector resolution. In 1993/1994 thirty two processor boards ran in parallel. Each board processes one event completely until a decision is reached. The hardware layout is described in detail in Section 7.

In order to reach a decision in the shortest possible time, the L4 algorithm is split into various logical modules, which are run only if a quantity calculated by the respective module is needed to reach this decision. The L4 modules use either fast algorithms designed specifically for the filter farm, or contain parts of the standard offline reconstruction program. The execution of the modules is controlled by a steering bank containing text in a steering language written explicitly for this purpose. The final decision is based on statements containing logical combinations of numerical or logical values. The event is either accepted or rejected if the statement is true.

Execution of the statement is terminated and the next

statement is executed as soon as a sub-condition is false. It is possible to run any statement in test mode without influence on the actual decision. This allows the evaluation of the effect of new statements with high statistics prior to activation and the flagging of particularly interesting events, e.g. for the online event display. In most cases, the first condition in a statement is simply a mask of L1 trigger bits. This scheme allows for high flexibility without changes in the program code and facilitates book-keeping as the steering bank is automatically stored in the H1 database.

A small fraction – typically 1% – of all rejected events is always kept for monitoring purposes.

In the 1993 runs the filter farm was mainly used to reject events with vertices outside of the nominal interaction region along the beam axis, which survived the relatively weak conditions set in the first level trigger. The largest reduction was achieved using charge division information from the trackers: In a first statement, a histogram of z -intercepts is evaluated. These are derived from the projection of straight lines defined by pairs of well separated wire hits in cells of the central jet chamber (CJC). If more than 50% of all entries are below $z = -75$ cm, the event is rejected. This condition rejects upstream beam-gas and beam-wall interactions. A similar algorithm evaluates multiple hits on neighbouring CJC wires. If the ratio of hit pairs with an absolute angle of less than 10° versus the beam direction to all hit pairs is greater 1/2, the event is rejected. Events with this topology are predominantly due to electron induced background originating from synchrotron radiation. These algorithms are very fast: both tests combined need an average of 8 ms on the processor boards and rejected 50–80% of the events triggered by tracker triggers in 1992. The full track reconstruction in the CJC is run on events passing the above criteria. Events with only positive charged tracks or no tracks at all in the beam interaction region are rejected. Three or more well reconstructed tracks originating from $z < -1$ m also lead to rejection of the event.

The BSET trigger described in Section 5.3.2 suffers from a large background due to particles hitting a single photo diode (mainly synchrotron radiation related). Events with a disproportionate fraction of the total stack energy in just one of the four photo diodes are rejected. In addition false BSET triggers from upstream proton beam background are rejected by the tracker cuts described previously. Muon triggers in the instrumented iron are verified by requiring a reconstructed track in the iron.

As can be seen in the above examples, the L4 filter farm has been rejecting background events based primarily on technical quantities. It has rejected an average of 70% of the input events. At higher luminosity rejection of beam-gas events in the nominal interaction region will become necessary. In addition, the increased number of filled bunches will necessitate the rejection of cosmic ray events.

The filter farm is not only used for event filtering purposes. As reconstructed data of the whole detector merges there for the first time, it is also well suited for monitoring

and calibration. The reconstruction modules fill monitor histograms which can be inspected online. Warning messages can also be sent to the central control console, informing the shift crew immediately of potential problems. Calibration data are sent to the data base for immediate use by the online reconstruction process.

5.6. Performance and outlook

With the above described system we reduced the high background rate at trigger level 1 to typically 26 Hz at the present luminosities delivered by HERA. 70% of these events were rejected by the level 4 event filter, so we ended up with a tape recording rate of 8 Hz at a overall dead time of the system of 8%.

The total rate of background events into the experiment due to proton beam losses from upstream was expected to be of order 50 kHz. In fact we measured at a total proton beam current of 0.8 mA (0.5% of the design value) an event rate of 225 Hz in the ToF scintillator wall, which scales with this expectation.

A proton-residual gas interaction rate of about 1 kHz/m can be calculated from the observed vacuum of 10^{-9} hPa and at design luminosity. This scales to 5 Hz within the interaction region (± 25 cm) and at the reduced luminosity condition mentioned above. We effectively observed a rate of about 2 Hz of such beam-gas events triggered with the central tracking triggers.

The rate of synchrotron radiation background turned out to be a bigger problem than expected. However by using the DC track trigger these events can easily be suppressed. For the low Q^2 deep inelastic neutral scattering events with the scattered electron observed in the BEMC this background is a more serious problem, only spatial correlation between BPC and BEMC and relative signal distributions in the BEMC photo diodes (see previous Section) give a significant reduction of this type of background.

Offline studies based on the data taken during the first year of HERA operation show that it is possible by setting more stringent coincidence requirements for the level 1 sub-triggers to run the system in the same manner (only level 1 and level 4 triggers) at 10 times higher beam currents without cutting significantly into physics acceptance and with the same performance concerning rates and dead times. However at design luminosity (100 times higher than our first year experience) we will have to tighten the requirements on the events in level 2 and 3 trigger systems. But it looks still possible to trigger with high acceptance for physics events, perhaps with the exception of the heavy quark production of which a large fraction of events have not enough transverse energy for the calorimetric triggers to fire and no or only low energy electrons or muons in the final state. Therefore they have to be triggered in the first level by central tracking information alone resulting in a high beam gas background from the nominal e-p interaction region. We will have to use topological criteria in the level 4 or even in level 2 or 3 to recognize these events.

6. Slow control

The slow control system of H1 [49] is designed to take care of all parameters of the experiment which would be constant in an ideal world. Except for central control and monitoring of all VME crates, all subdetectors described above are equipped with a slow control system of their own. All systems use VME crates controlled by Macintosh or OS-9 computers and some of them use a VME-controlled multichannel slow control system developed at H1 [50]. The integration of subsystems is achieved in two ways, a simple hardware alarm system and a computer control network (CCN). A combined database is used for maintenance of static data and storage of measurements.

Throughout the slow control system we use the notions of slow channel (SC) and slow event (SE) [51]. A slow channel is a single measurable quantity of a single signal type of a single physical channel (e.g. a real setting of a high voltage power supply channel, or the value loaded into this channel). Each SC is uniquely identified by its code (ID). All slow channels are first initialized by their subsystem computer according to the central database. A microevent occurs when a significantly new result is obtained from the measurement on a SC. Microevents are accumulated in their slow event buffer until the status of some SC has changed, the time allowed for a SE accumulation has expired, the command to send a SE was received or the maximum number of microevents within a SE has been reached. As a result of any of the above conditions (SE triggers) a slow event is sent to the central slow control computer.

We use a relational database management system for the maintenance of slow control data. We use the structured query language (ANSI SQL) for the purpose of data integrity, control of access and commitment, and for queries. The complete history of the databases is kept. Any set of reports from queries can be automatically formatted into H1 standard records suitable for production programs. Slow events are stored in two standard files. The slow event archive file uses keyed access to SEs. Both of these history files are zero-suppressed in the sense of microevent defi-

inition. We have a good interactive access to slow control data stored on the mainframe IBM computer. A menu tree can be used to guide casual users. Remote access to all databases and history files is made transparent by a TCP/IP database server.

The control network consists of subsystem control computers (Macintosh and OS-9) attached to different detector parts (Fig. 19). They are connected via Ethernet (TCP/IP). CCN is used to monitor all parameters of H1. All slow control computers produce SEs and transfer them to the central slow control (CSC) computer. The CSC computer provides data for the online display of the detector status [52] running on Macintosh computers. SEs are also injected into main data acquisition event data stream. On the mainframe IBM computer they are copied to the history files. The CSC computer itself monitors some 200 VME-crates and other devices not linked to a particular subdetector.

Hardware alarms do not depend on computers. Only hard-wired combinatorial logic is involved to handle critical situations immediately (e.g. to switch off high voltage power supplies). The central logic [53] uses open/close switch signals. It is connected to the experiment via a routing array which makes it possible to receive input from or deliver output to any location within H1. The central logic drives an alarm signalization panel in the control room and provides status flags read out by the data acquisition and included into the event data.

In summary, the hardware alarm system presently monitors some 170 signals. It works reliably and can readily accommodate new input or output anywhere within the whole experiment. The only change foreseen is automatic interaction with the accelerator.

7. The data acquisition system

This Section concentrates on the central part of the H1 data acquisition system, the front-end readout and triggering subsystems having been dealt with extensively in previous Sections.

From the real-time computational point of view, a total of over a quarter of a million analog channels are read-out and digitized, resulting in some 3 Mbyte of raw digitized information for a triggered event. As the time between successive electron-proton bunch crossings is just 96 ns, various levels of hardware triggering, software filtering and digital compression are employed before reducing final data sizes to acceptable storage-media recording rates. For the data acquisition several hundred processing elements are embedded largely within the IEEE VMEbus standard [54]. Descriptions of the system also exist elsewhere [55,56].

Fig. 20 summarises the overall data acquisition system and the key rates at full HERA design luminosity. Information is digitized and read-out in parallel from many subdetector partitions before being finally merged. Four main levels of hardware triggering and software filtering can be enabled

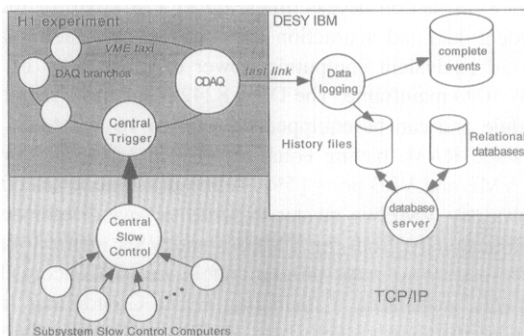


Fig. 19. Flow of slow control data within H1. The data flow between the database server and slow control computers over TCP/IP has been omitted.

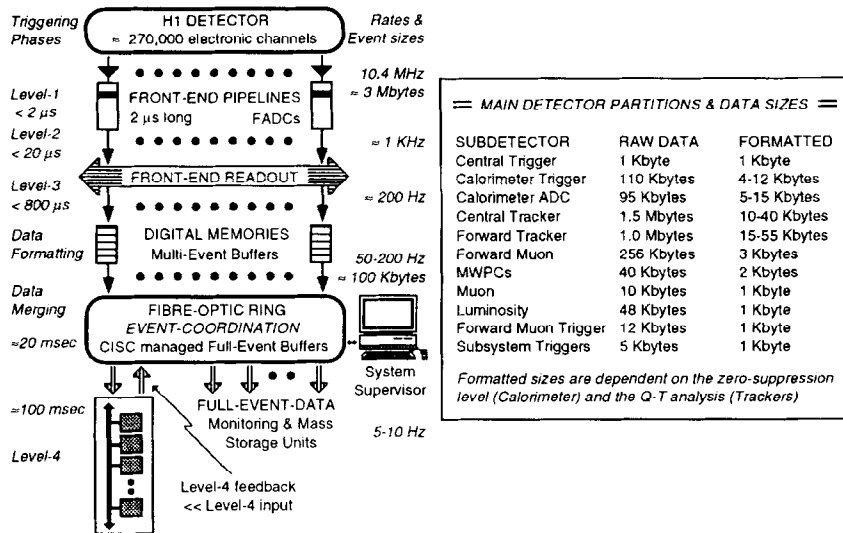


Fig. 20. Overview of the H1 data acquisition system.

on all or part of the various detector partitions. In parallel data compression and formatting reduce the 3 Mbyte of raw data to event sizes of between 50 kbyte and 100 kbyte so that final data recording rates are restricted, at present, to a maximum 1.2 Mbyte/s. The first level (L1) pipelined triggering system selects initial candidates for data processing from the background. After a L1 accept the front-end pipelines are held. Dead-time then begins. A more refined hardwired L2 decision, based on combined information, can then be activated within 20 μ s. Front-end electronics readout is not initiated until an early-level triggering decision is made whereupon each component has a maximum digitization time of 800 μ s before the pipelines are re-enabled; a large amount of the data compression also takes place during this phase. A third level of filtering can be enabled so that should readout commence the pipelines are immediately reactivated if a L3 reject occurs.

In logical structure the detector components are merged, in parallel, into individual subdetector VMEbus crates which each contain a readout controller and memory buffer plus a fibre optic link to a coordinating event management task. A parallel array of RISC processors provides the fourth level of software-coded filtering once all of the full-event information is combined over the fibre-optics [48]. At all stages workstation intervention provides for data monitoring and detector control. To avoid saturation on global VMEbusses, extensive use is made of the local VSB specification [57]. To minimise any further dead time contributions, memory buffering is provided at the key data processing stages. Finally a local area network (Ethernet) caters for the relatively slow exchange of general operating conditions, files and even event-records between different subsystems. This also serves the external international community with current status and event information over wide-area networks.

7.1. System components

To provide a coherently managed system, between over 200 electronics crates, a baseline set of standards was established to ease maintenance and software development overheads.

7.1.1. Basic hardware components

For general-purpose real-time control within VMEbus, a common 68020/30/40 series processor card was selected [26]. On-board memory is dual-ported so that it can be accessed externally from the VMEbus (for communication) as well as internally from the processor itself. VSB local bus access can be extended to memory boards in adjacent crates but is never used as an inter-crate connection. For even more calculation-intensive applications RISC processor-based modules are employed. The RAID 8235/8239 is a single-width VMEbus/VSB board based on the MIPS R3000 processor (25/40 MHz clock) and the R3010 Floating-Point Accelerator with up to 32 Mbyte of onboard DRAM [58]. To enhance memory bandwidths and reduce instruction access times, up to 128 kbyte of independent data and instruction cache ensure that each board has an equivalent computing power of up to 80% of an IBM 3090 mainframe. The DPM 8242 is the basic memory module and can be equipped with up to 16 Mbyte of 70 ns static RAM, having equal priority in arbitration from the VME and VSB ports [59]. A broadcast mode selection allows any VMEbus master to write to several memories simultaneously. Both the VMEbus and VSB memory base addresses are software programmable via VME accessible registers, permitting a managing Event Coordinator task (see later) to switch units between different events. Due to their graphics-user-interface and open NuBus architecture, Macintosh computers are used extensively for the purpose of

software development and operator control. A maximum of 24 VMEbus crates can be mapped directly onto each Macintosh via MacVEE and Micron, MacVEE interface card resident on NuBus [60]. No sophisticated protocol needs to be initialised, unlike other DMA-based connections.

7.1.2. VMEtaxi

In many of the front-end subsystems the standard VICbus is used to interconnect crates [61]. However for coordinating the fast data acquisition transmission protocol between the different readout subsystems, VMEtaxi modules are employed [62]. These can connect VMEbus crates up to several kilometres with fibre-optics. Fig. 21 illustrates the basic philosophy. All boards are interconnected with multimode optic fibres to form a ring, using AMD 7968/7969 TAXI-chip transmitter/receiver pairs. Because of this, there is theoretically no limit on the number of such devices which can be interconnected within a single ring; in practice one is limited by the software overhead in setting up transfers. Each single-width board has a CPU controller and single level VMEbus arbiter. The software protocol, discussed further in the following Sections, is purpose-written and optimised for speed and efficiency in a data acquisition environment; no FDDI or similar networking protocol is adopted. In setting up transfers between any two crates, an initial description packet is sent around the ring; those modules not engaged in the subsequent activity can enable by-pass registers so as to establish a direct connection between the two VMEtaxis that are involved, analogous with SCI [63]. During the early stages of data-taking, a 25 MHz 68020-based board was used with 125 MHz taxi chips. Upgraded Mark-2 modules are now installed which exploit 50 MHz 68030 processors and either 175 MHz or 250 MHz taxi chips. By driving double-links in parallel there is the potential for 55 Mbyte/s point-to-point data transfers between crates up to distances of several km. The link reliability has been tested to a bit error rate of less than 1 in 10^{13} . Program memory is provided for by 128 kbyte of on-board fast static RAM with an additional 2 Mbyte of on-board extension static RAM accessible over the VMEbus by external processors. On-board EPROM and EEPROM provide for firmware storage and

configuration parameters. VME64 and VSB block transfer modes are realised on the Mark-2 modules with XILINX gate arrays.

7.1.3. Software

The architectural structure of the hardware, discussed in the following Section, defines how the software is written and developed. Dedicated tasks run on dedicated processors throughout the VMEbus system with operator intervention provided for via graphics-orientated computers such as Macintosh. Different languages and approaches are used depending on the application being developed. Much of the online data acquisition systems code which executes on 68000 series microprocessors, within the VMEbus, is written in either C or Assembler. Final-level filtering algorithms, which execute on the R3000 boards, have large code resources originating offline and written in Fortran [48]. Control programs which run on the Macintosh computers exploit the latest object-orientated and graphics-based packages currently on the market [64]. It can be seen that the Macintosh provides a convenient integral component in both software development and operator-control. In order to encompass the framework of VMEbus, extra tools have been developed to ease the integration into the VMEbus [65]. As a result, no formal operating system is required to run on the VMEbus boards; all basic functions can be controlled from a Macintosh via external directives through dual-ported mailbox memories. In order to enhance information exchange between control computers a dedicated package has been written based on international networking protocols [66]; this has the added advantage of enabling the complete system to be monitored from external laboratories and institutes.

7.2. System Integration

By convention the data acquisition system breaks down into three main categories for the purpose of central coordination and management. First there are the front-end "producers" of data; the end result of extensive electronics digitization from the subdetectors or "branches". Second, the data are merged and distributed to several full-event "consumers"; subsystems which monitor and record the data onto permanent storage media. Third, the system is initiated and controlled via external processes for overall system supervision and operator intervention. Fig. 22 shows the physical layout of the complete system, managed centrally through several layers of software protocol, purpose-written around the VMEtaxi fibre-optic ring [67]. Common, shared, memory blocks provide for the communication between all system processors and external computer stations. The master of the ring executes the "Event Coordinator" task, controlling the whole sequence of management processes. A separate object module provides a software library to interface the individual subsystem elements, with features ranging from full module testing and control through to basic buffer management and system coordination.

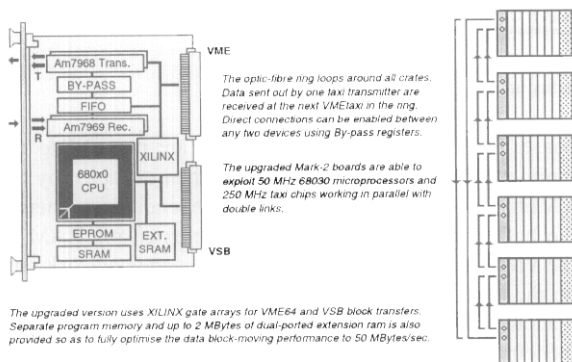


Fig. 21. VMEtaxi fundamentals.

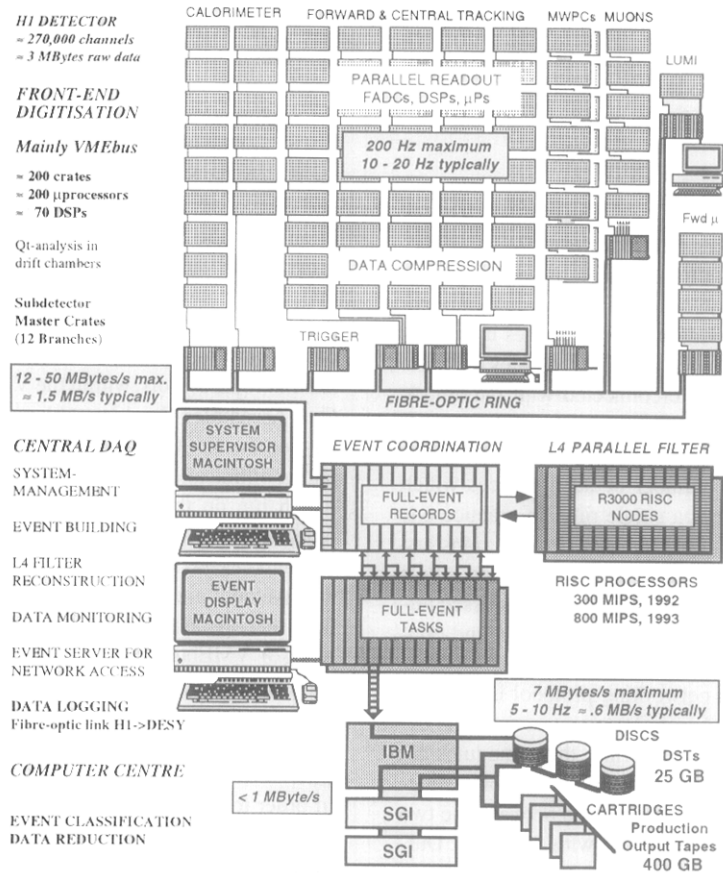


Fig. 22. Physical layout of the key features of the H1 data acquisition system. See text for details.

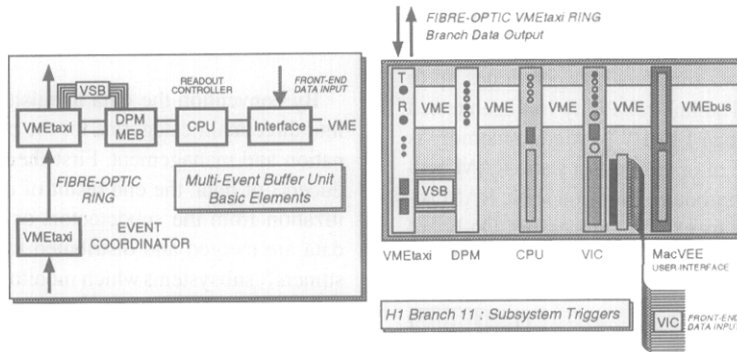


Fig. 23. Multi-event buffer units.

7.2.1. The architecture of the front-end producers

The readout system of each branch is autonomous up to and including a central subdetector VMEbus crate. Each central subdetector crate contains a dedicated supervisory readout controller, a multi-event buffer (MEB), a VMEtaxi and any input drivers necessary to access the data (Fig. 23). Consequently the design allows a particular subdetector to be decoupled from the rest of the system, during installation and test phases, and does not exclude the use of other

busses for front-end digitization. Data are placed into the multi-event buffer over VMEbus and then extracted by the VMEtaxi either over VSB or locally, depending on whether the buffer uses a DPM or exploits the extension RAM of the VMEtaxi. The Event Coordinator management task runs on the master VMEtaxi of the ring and interacts with each readout controller via shared memory blocks. Before commencing data acquisition, the Event Coordinator is responsible for hardware recognition and initialization of the var-

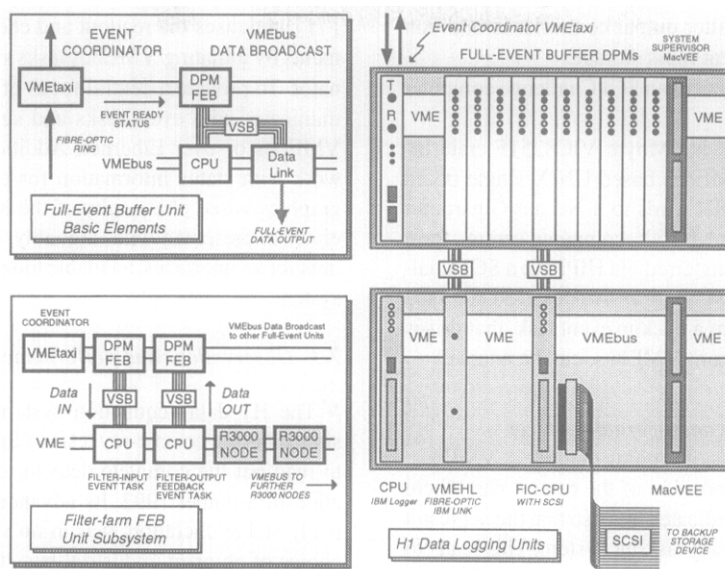


Fig. 24. Full event buffer units.

ious branches. During acquisition, when it is free for event building, it searches the subdetector multi-event buffers for the next event. When all branches are ready with the same event number, the separate banks are transferred via the optical ring into a full-event buffering system. On completion, each corresponding buffer is released. A subdetector crate may also contain additional processors for data reduction, an interface to a subdetector monitoring computer and a subsystem trigger controller (STC). All STCs are interfaced to a dedicated central trigger controller which, in turn, coordinates the sequence of all hardware triggering levels together with obtaining information from the HERA machine [68]. Each STC provides signal ports for the component electronics and communicates with the readout through VMEbus read-write cycles and interrupts. A consequence of this is that the Event Coordinator needs no hardwired connection with the central trigger controller itself; all management sequences are handled by software, so providing a portable solution to any large multi-crate VMEbus system [67].

At the subdetector branch level, the software library provides multi-event-unit routines catering for initialization, accessing status information, requesting buffers and signalling when event data are ready for merging. Readout error codes are normally indicated as standard parameters, but messages can be sent through the system in standard ASCII format to describe branch-specific anomalies. Fig. 23 also shows how the protocol has been transparently mapped from a main branch through to a sub-branch structure by incorporating standard VIC links to merge smaller subsystem components.

7.2.2. The management of full-event consumers

As the Event Coordinator VMEtaxi builds full-event records it simultaneously broadcasts them along its VMEbus to dual-ported memories associated with parallel sets

of "full-event units". Event tasks are performed by connecting the unit processors with their respective full-event buffer (FEB) memories via VSB in order to minimise any bandwidth overheads (Fig. 24). Since the memory has read/write access from both the event task processors and the Event Coordinator, full-event units need not only be "consumers" of data. An event unit can also become a "producer" of data, "feeding-back" data into the system. Consumers are able to determine which data they wish to receive, i.e. directly built events from the front-end branches or data fed-back into the system from, for example, a parallel filter farm. All this is handled modularly by the software protocol and its associated library of routines.

Typical full-event tasks are local data-logging, event display, data monitoring and histogramming. A more sophisticated form of unit is the fourth level filter "farm" consisting of many MIPS series processor "nodes" working in parallel. Each node executes the same algorithm independently on different events. This provides not only a final level of triggering but a further stage of data processing and online reconstruction, used for online event display [69].

Event records are passed to the different nodes under control of 3 filter input controllers, which communicate with the Event Coordinator as normal consumer full-event tasks. When a node is free it signals this to its filter input task which waits for an event ready in its full-event buffer. The data are then extracted over the VSB and sent to the free node, releasing that particular buffer and enabling a further node to be serviced. When a node has finished processing an event it signals completion to the filter output controller (a "feedback" event task). The latter then decides whether to pass the event back into the central system managed by the Event Coordinator and frees the node buffer for further processing. As a full-event unit, the parallel filter can be easily

enabled or disabled. The filter output controller in addition handles output to permanent mass storage.

Final event records are sent to an SGI Challenge computer some 3 km distant [70].

The data is transferred via 4Mbyte VIC8251F crate interconnects to FORCE VMEbus based UNIX single board computers with SBUS FDDI cards to a Netstar Gigarouter in the 3 km distant central DESY computer centre, from where the data is finally transferred via HIPPI to a SGI Challenge mainframe and via SCSI to an Ampex DST800 tape robot. In case of link failure a backup event task, that drives a storage device directly from VMEbus, can be enabled.

7.2.3. System supervision and operator-control

The H1 system is capable of running entirely in VMEbus; Fig. 25 illustrates the composition of the central part where dedicated processors run dedicated tasks so that the net result is one of a conventional multi-tasking system. This leads to a natural division of tasks and processes. The primary tasks of data acquisition are performed by the subsystem readout controllers, event builders, filter control tasks and event units, all managed by the Event Coordinator. All fast processing and readout is done within VMEbus. An exhaustive software library caters for external control by providing a full set of routines for system configuration, testing, system-status and monitoring [67]. NuBus-based Macintosh computers take over the responsibility of program development and run-time operator-control. The System Supervisor Mac

[71] initialises the readout and checks the status of all elements by initiating VMEbus tasks such as the Event Coordinator. To provide a central focus of monitoring it also communicates with event tasks and subsystems either through VMEbus or over Ethernet. Additionally it serves the network with status information for external monitoring. The graphics-based philosophy of the Mac ensures that the operator is presented with, arguably, one of the most human-interactive interfaces, available today, to a complex real-time system.

7.3. Observations and performance

The H1 data acquisition system was initially commissioned during cosmic-ray tests in Spring 1991 and then used to read out the complete detector during first HERA operation in Summer 1992. Its advanced preparation, and relatively stable operation, was in no small measure due to the choice of an open, industrial bus-standard and the incorporation of modern commercially available hardware and software where suitable. Of particular note has been the extensive use of the networking facilities in addition to the main data flow. The ability to control and monitor the system externally, even from the latest generation of portable notebook computers, has been extensively capitalised upon.

From the master VMEtaxi the system can manage up to 32 branches and 16 full-event units, including the parallel filter farm, providing status information and accepting control command sequences from the System Supervisor Macintosh. Presently events of up to 100 kbyte can be coordinated from 12 branches at rates up to 200 Hz using the Mark-2 VMEtaxi modules, depending on the filter farm rejection rate. The primary sources of dead time remain at the front-end, where future injections of greater processing and refined triggers are made more comfortable by working within an international bus standard.

8. Off-line data handling and simulation

This Section concentrates on the off-line data handling, quasi-online data reconstruction, event simulation and the H1 analysis environment.

8.1. Off-line computing

An overview of the H1 offline computing environment is given in Fig. 26. The H1 experiment is using two multiprocessor SGI Challenge series computers for all computing purposes [72]. They are connected to the DESY computing infrastructure via fast UltraNet, HIPPI, and FDDI links as well as Ethernet. Fast access to data both on disks and tapes is provided. The disk space amounts to about 500 GB connected via SCSI interfaces. The access to the data stored on disk allows many users to analyze the data simultaneously, thus offering an efficient environment for physics analysis. Major tape service is provided by four Storagetek Automatic

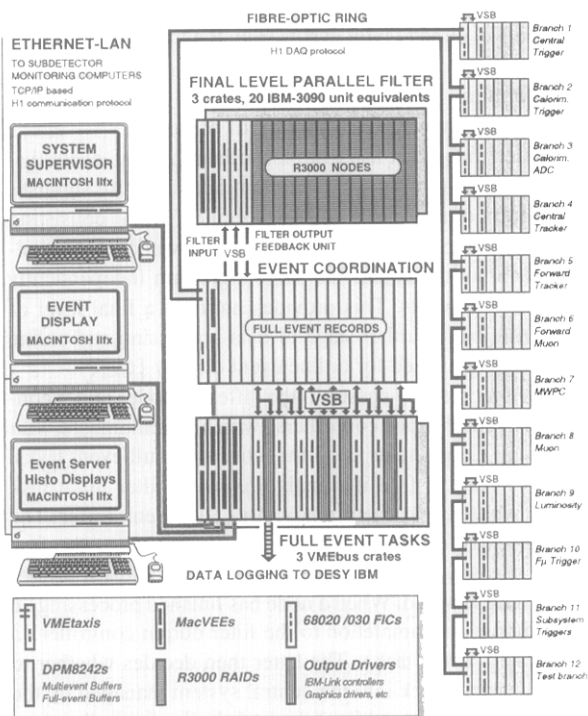


Fig. 25. Physical composition of the central part of the H1 data acquisition system as during the data taking periods of 1993 and 1994.

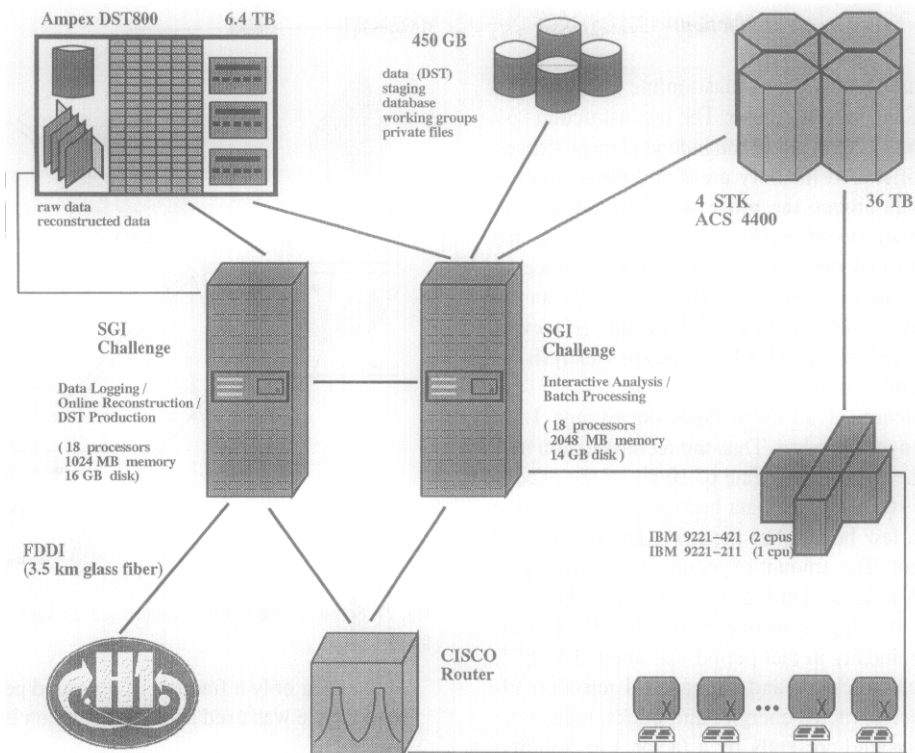


Fig. 26. H1 off-line computing environment

Cartridge Systems with a total capacity of about 35 TB, directly accessible from the SGI Challenge using the Open Storage Manager software. Mass data are also kept on an Ampex TeraStore mass storage system, equipped with 3 helical scan D2 recorders and connected to the SGI Challenge via SCSI interfaces. The total capacity of the Ampex system amounts to 6 TB. Multi-user access to data on tape is also offered by an efficient staging mechanism. Export of data is performed via 3490 and Exabytes cartridges.

During data taking, one of the SGI computers is dedicated to the data logging and online reconstruction tasks. The analysis of data is performed on the second SGI Challenge computer and partly on the IBM mainframe. Several institutes have also installed RISC processor based workstations at DESY for analysis purposes, connected to the local network facilities.

Care has been taken from the beginning that all offline processing of the data and simulation was portable between DESY and external institutes. Meanwhile many of these institutes have installed the complete offline program chain and participate in simulation and data analysis. More than half of the detailed detector simulated data were produced in external institutes. Furthermore, most institutes are connected to DESY via fast network links.

H1 uses the dynamic memory management package BOS [73] for its software. A general input/output package, FPACK [74], was written in order to have a simple and unique system for all data transfer in the experiment. It con-

tains automatic wordformat conversions between different machine representations (IBM,VAX,DEC,IEEE), includes record selection options and supports event directory based fast access to data. A database package was developed and is used to store run dependent data and Monte Carlo information. Further, the code manager CMZ [75] is used for the H1 software packages. A set of simple but solid rules, complemented by the necessary subdivision of responsibilities and the imposing of discipline, has created a successful and efficient environment for code development in this large collaboration. Details on code management with CMZ in H1 can be found in Ref. [75].

An important aspect of the software is the concept of modularity [76]. Modules are self-contained sets of routines with clear I/O interfaces. They take care of their own initialization upon first call. Modules communicate to each other only via BOS banks. A larger program, such as the reconstruction program, consists of a simple series of module calls. Purpose written utility software performs automatic book-keeping of used input and created output BOS banks and guarantees the internal consistency of the data after re-processing of modules. The dynamic memory management package BOS includes modularity oriented functions to support this scheme.

H1 also uses an entity relationship model as a basis for data structures of all event data. A data management tool DATMAN [77] provides an easy and userfriendly access to the data.

8.2. Data reconstruction and reduction

The H1 data are reconstructed quasi-online [70] on an 18 processor SGI Challenge computer. The reconstruction task runs in parallel up to 25 identical and independent processes, whereby a set of shared memory areas and semaphores is used to share data among the processes. The raw and reconstructed data are stored on D2 tapes on a dedicated tape robot. During normal operation, the data taking proceeds with an average rate of about 500 KB/s, leading to an expected yearly data volume of about 5 TB. A part of the event information is stored on disk (DST) for physics analysis for the full data taking period.

The reconstruction of an event takes on average 1.5 s on a SGI Challenge processor. Thus the reconstruction task can cope with the data logging rate of 10 Hz of the experiment. In all, the reconstructed data become available to the users typically a few hours after the raw data are recorded by the experiment. The amount of recorded data by experiments at HERA is large. During the 1994 data taking period about 7×10^7 triggers were recorded by H1. The total integrated luminosity in that period was about 3.5 pb^{-1} . Off-line event classification and background rejection filters, based on reconstructed energies and tracks, reduce the amount of background presently by a factor 3 to 5 during reconstruction. Background rejection filters include cosmic muon and muon-halo filters, recognition of coherent noise patterns and filters for beam-wall and beam-gas collisions originating from outside the detector.

8.3. Event simulation

A complete detector simulation program has been assembled within the GEANT [78] framework. The geometry of the full detector and the beamline within $\pm 100 \text{ m}$ around the interaction region is implemented with two different levels of detail, called fine and coarse granularities. For the fine granularity the longitudinal structure of all calorimeter stacks is implemented layer by layer, whereas for the coarse geometry a calorimeter stack is implemented as a block of properly mixed homogeneous material with no longitudinal structure. For the tracking detectors separate volumes are implemented for each active cell (wire) for the detailed geometry, whereas for the coarse geometry an entire gas volume is treated as one volume. For accurate detector response, particularly in the detailed geometry option, the tracking cutoff parameters for the kinetic energies have to be set as low as 1 MeV. This leads to simulation times of the order of 200 s for a typical low Q^2 deep inelastic event on a SGI Challenge processor. Three strategies were followed to tackle this large CPU time consumption for event simulation:

- The time consuming part of the actual tracking of particles through the geometry was strictly separated from the digitization part of the detector response. Run dependent detector effects and the actually achieved resolutions can easily be adjusted by reprocessing the digitization part

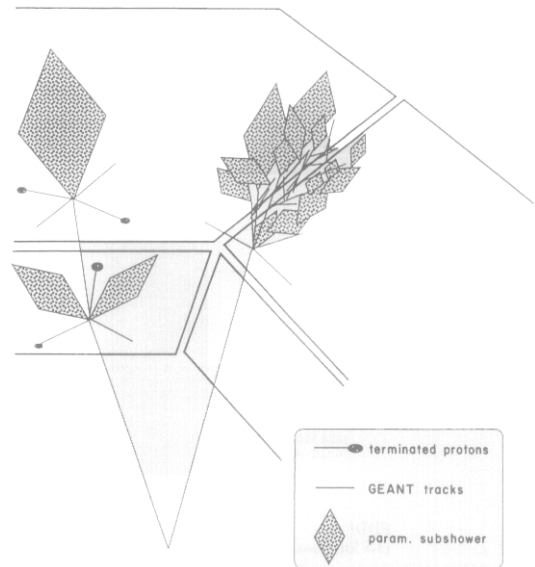


Fig. 27. Schematic view of the parametrized shower simulation in a coarse geometry.

only, using only a fraction of a second per event. A similar scheme was used for the simulation of the trigger response.

- A book-keeping is made of all energy depositions in the detector, both for visible and invisible (nuclear breakup, neutrinos, slow neutrons) energies, and both in active and dead detector regions [79]. This allows to reconstruct the calorimeter response after simulation with simple response functions, which are basically sums over the smeared true energy depositions. The absolute energy scale can thus be reconstructed correctly, which gives an important handle for testing the reconstruction programs and also to understand the behaviour of a non-compensating calorimeter.
- A fast but accurate energy shower parametrization [80,81] was developed. This so-called H1FAST mode was included into the GEANT framework. The main idea is sketched in Fig. 27. The time consuming part of the full shower development in the detailed geometry is replaced by a shower parametrization in the coarse geometry leading to reduction of the CPU time consumption by a factor 10. Showers which cross crack boundaries are simulated in detail, in order to keep accuracy.

8.4. Physics analysis

The visual aspect of the physics analysis is mainly handled by a purpose written general system for graphics applications, baptized LOOK [73]. The aim is to have one – and only one – graphics package for all graphical applications: event display, histogramming, analysis, etc. LOOK can be considered as a layer between the user application and low level graphics functions, for which at present GKS functions are used. LOOK organizes the management of the display

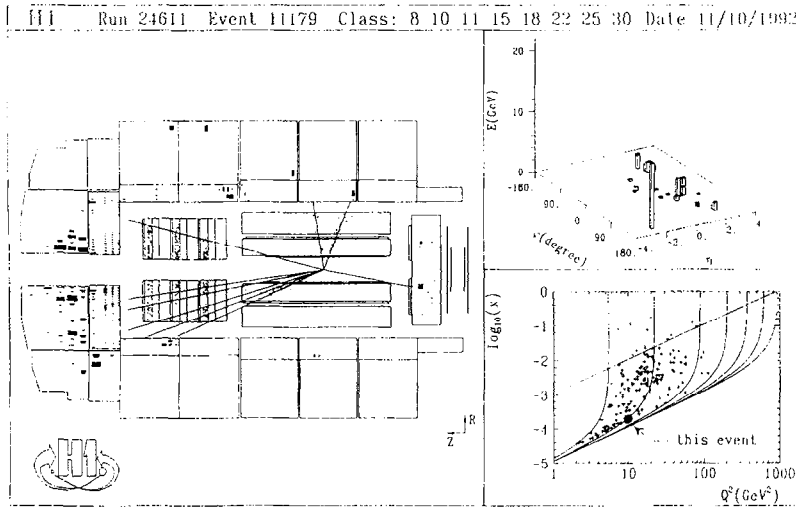


Fig. 28. Physics analysis with LOOK.

and e.g. hardcopy devices. It further contains a histogram package and a powerful command processor and is portable to many platforms. The H1 event display program, HIED, is an application based on LOOK. Fig. 28 shows an example of an event display and histogram analysis combined in one session. LOOK can be used for interactive analysis, e.g. n -tuple analysis of data. Also PAW [82] is used for interactive analysis.

The program HIPHAN is a tool to access event data and simplify physics analysis programs. The data are filled in internal event buffers called Q-vectors, which are accessible in simple Fortran DO-loops. Thus the user does not need to know the –sometimes complicated– underlying bank structure of the data. HIPHAN further contains tools for particle identification, secondary vertex fitting, jet finding and analysis, determining kinematic variables of deep inelastic event candidates, etc.

9. Summary of first operation at HERA

The successful operation of the H1 detector during the first years of HERA is evidenced by the many publications [83] which resulted from it.

The measurement of the total photoproduction cross-section [29] relied mainly on the luminosity monitor and electron tagger. It showed that the novel technique of monitoring luminosity via the $ep \rightarrow e\gamma$ bremsstrahlung process combined with on-line background subtraction using electron pilot bunches can be used meaningfully. The electron tagger signal alone provides a fairly clean trigger for all photoproduction physics. Supplemented with tracker and calorimeter information at the trigger and reconstruction level the prominent beam gas background can be removed completely, as demonstrated in the analysis for hard photon scattering [30]. Fig. 29 shows an event typical of this type of processes.

The total cross-section measurement with the electron tagger was cross-checked with data triggered only by the z -vertex trigger (see Section 5.3.1), which required a minimum number of tracks from a common vertex in the interaction region. Though photoproduction events from a different range of Q^2 and y are accepted by this trigger, a detailed understanding of this trigger and its dependence on chamber efficiency, noise, crosstalk, track transverse momentum p_t and energy loss is need, as is also a subtraction of proton pilot bunch data. The results are found to nicely confirm the electron tagger analysis.

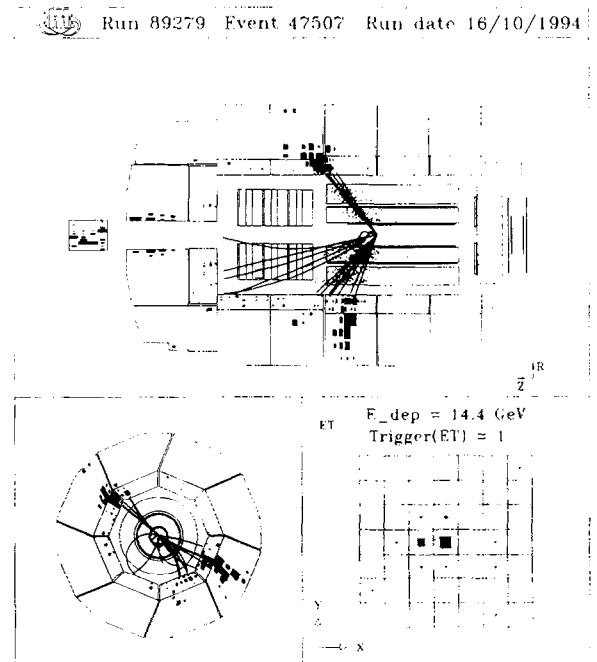


Fig. 29. Typical two jet event from γ - g fusion tagged by an electron in the tagger.

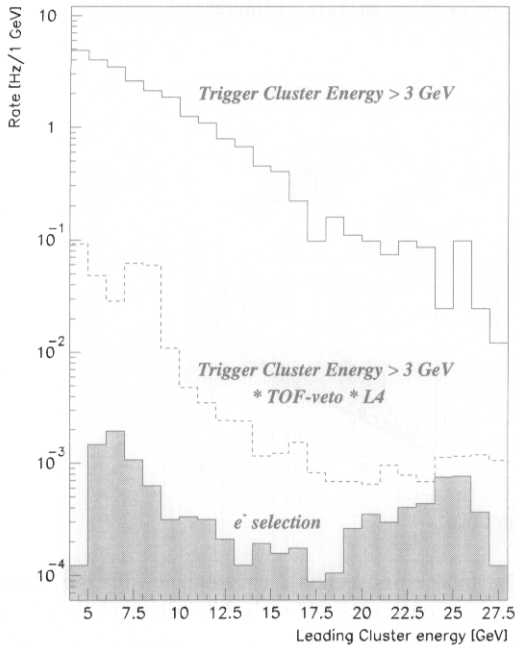


Fig. 30. Absolute trigger rates recorded in the backward electromagnetic calorimeter in function of cluster energy at different trigger and reconstruction levels.

The above examples were cited to emphasize again one of the stronger points of the H1 detector, which has been explained in more detail in the trigger Section above, namely the ability to trigger on the soft physics while not losing the deep inelastic events or vice versa. The use of topological

information rather than thresholds on individual detectors, is a major step forward and will ease data taking at higher luminosities.

The first measurement of deep inelastic scattering in the new kinematic domain accessible to HERA required an understanding of the energy response of the backward electromagnetic calorimeter (BEMC) and the backward and central parts of the LAr calorimeter. Fig. 30 shows the spectrum of energy clusters in the BEMC. Without additional constraints the trigger rate amounts to a few Hz/GeV even at the low beam intensities achieved so far. The observed rate is dominated by proton induced background hitting the rear part of the calorimeter. The rate can be reduced by almost two orders of magnitude by a simple timing requirement in the time-of-flight detector. In the analysis simple event topology and track matching cuts produce an almost background free electron spectrum for energies exceeding 15 GeV. Below that value fake electron signatures from photoproduction hadronic final states become dominant. These can be rejected by active electron identification tools (like shower shape analysis). The so-called kinematic peak, a feature discussed in our first publication on deep inelastic scattering at low x [84], and also in Section 3.2 of Ref. [9] in the context of the BEMC calibration, is clearly seen in this spectrum.

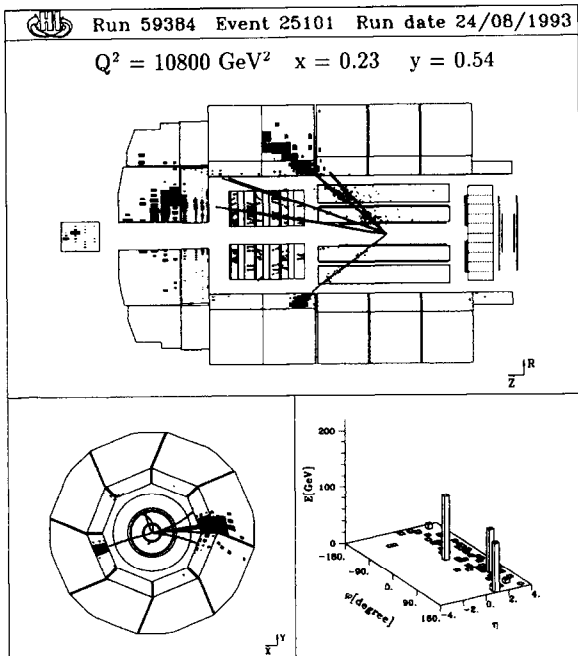


Fig. 31. Typical high Q^2 event with both the scattered electron and the hadronic recoil jet observed in the LAr calorimeter.

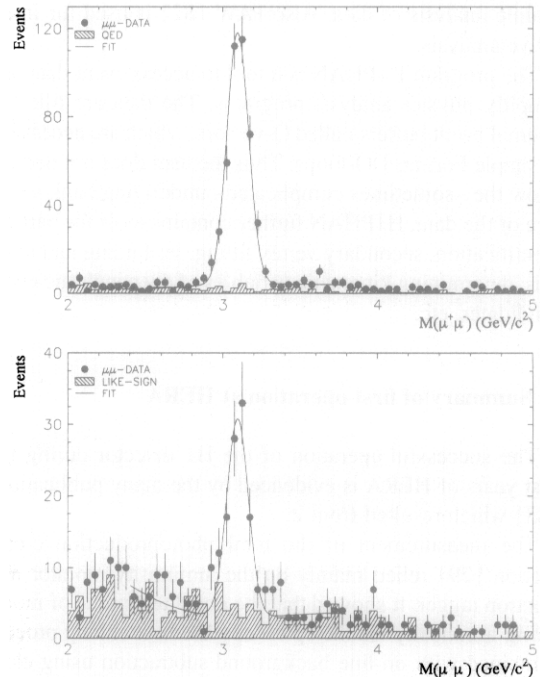


Fig. 32. Invariant mass distribution of elastically (bottom) produced $\mu^+\mu^-$ pairs in J/Ψ photoproduction. The curve is a fit of a Gaussian plus a polynomial background to the J/Ψ mass region. The shaded histogram shows the contribution of QED lepton pairs (top figure) and the contribution of like sign muon pairs (bottom figure). The maximum of the fit is at 3.10 ± 0.01 GeV with a width of 76 MeV, and at 3.10 ± 0.01 GeV with a width of 65 MeV for the top and bottom distributions respectively, the detector simulation yielding in each case a width of respectively 65 MeV and 60 MeV.

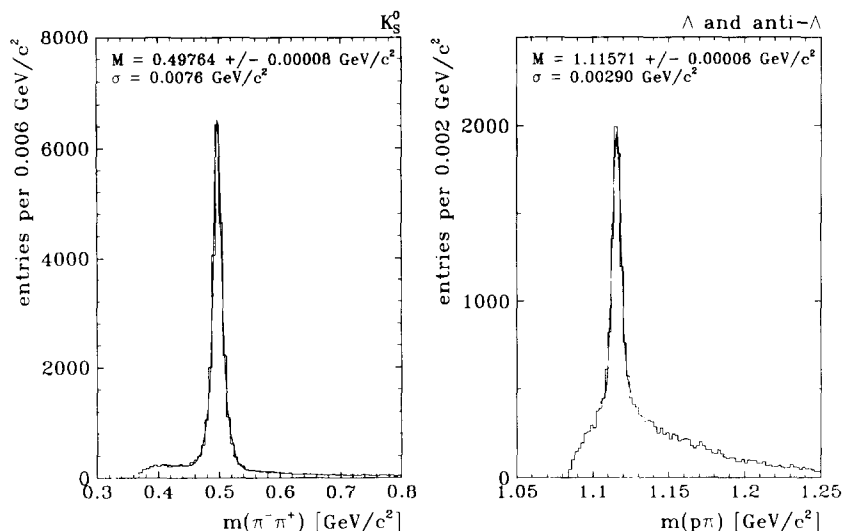


Fig. 33. K_s^0 (left) and $\Lambda(\bar{\Lambda})$ (right) signal observed in the central jet chamber.

Events with a hadronic final state [85] are of the type shown in Fig. 31. The check of the balance in transverse momentum (see Figs. 32 and 39 of Ref. [9]) entails the understanding of both the hadronic as well as the electromagnetic part of the liquid argon calorimeter, and the link between tracker and calorimeter information.

On the technical side, the high stability, reliability and small number of dead channels in the liquid argon calorimeter deserve to be singled out. The noise level was found to be low enough to extend its use down to quite low energies.

The digital muon system and the muon trigger behave as expected. Fig. 32 shows the invariant $\mu^+\mu^-$ mass spectrum for elastic and inelastic photoproduction of J/Ψ mesons, with a prominent peak at the mass of the J/Ψ meson. These events were mostly triggered and identified by the muon system.

Fig. 33 shows the resolution of the K_s^0 peak in the $\pi^+\pi^-$ mass spectrum and of the $\Lambda(\bar{\Lambda})$ signal. This may serve as evidence, that the isolation of J/Ψ , D^* -tagging etc. is feasible, once sufficient statistics is available. The $J/\Psi \rightarrow \mu^+\mu^-$ candidates found prove that the tracker muon link can be made.

On the software side the online filtering and reconstruction concepts have permitted a fast access to the data, and also their quick reduction and dissemination to the various analysis centres.

10. Upgrade program

During the winter shutdown 1994–1995 the detector was moved out of the beam and several upgrade operations were performed, as listed below:

- the beam pipe was replaced by one of smaller diameter ($\varnothing 9$ cm) made of aluminum, 2% of X_0 at 90° .

- a set of trackers made of silicon detectors (CST and BST) was installed between the beam-pipe and the CTD, the CST (see Refs. [15,86,87]) covering the central angular region for improved vertex detection and the BST (see Refs. [15,86,88–90]) covering the rear angular region to improve reconstruction of rear-going small angle tracks.
- the BWPC was replaced by a drift chamber (Backward Drift Chamber BDC) made of eight layers. The layers are arranged in four different stereo views. It has a much improved resolution capability and furthermore provides trigger information for the H1 level 1 trigger. For details see Ref. [86].
- the BEMC was replaced by a lead-scintillating fiber calorimeter (SpaCal) providing improved energy and spatial resolution for electrons down to angles of 177° . This calorimeter consists of two sections, each $\sim 1\lambda$ deep, the first one for detection of electromagnetic showers and the second one for measuring the electromagnetic energy leakage from the e.m. section as well as a determining the hadronic energy flow in the backward region. Furthermore, the latter section provides the H1 detector with a time-of-flight veto on proton beam induced background from upstream, replacing the ToF system described in Section 2.7.1 of Ref. [9]. Fast signals are used for triggering. For more details see Refs. [86,91–96].
- downstream of the proton beam a forward proton spectrometer (FPS) was added. It consists of stations at 81 m and 90 m, where scintillating fibre hodoscopes can be moved close to the circulating beam by employing the Roman Pot technique. Protons which cross both stations generate a trigger signal which is added to the H1 trigger mix. Two more stations at 63 m and 80 m are planned for 1997. More details can be found in [97–99].

- at 107 m from the interaction point, downstream of the proton beam, a lead-scintillating fiber calorimeter was installed. Originally developed at CERN for the LAA project and subsequently used by the UA89 experiment, its purpose is to measure the energies and angles of neutrons produced in DIS interactions. It has a good acceptance for neutrons with a production angle less than 1 mrad. For more details refer to Refs. [100–105].
- the second level triggers mentioned in Section 5.4 were installed and tested using real data.

Acknowledgements

We appreciate the immense effort of the engineers and technicians of the participating laboratories who designed, constructed and maintain the detector. We are grateful to the HERA machine group whose outstanding efforts contribute to making this experiment possible. We thank the funding agencies for financial support. The non-DESY members of the collaboration also express their thanks the DESY directorate for the hospitality extended to them. We acknowledge the help of DESY and CERN in providing test beam time for the many calibration runs. The help of the computing centres at DESY and at CERN in the test and running phases is highly appreciated.

References

- [1] M. Breidenbach et al., Phys. Rev. Lett. 23 (1969) 935; 1990 Nobel prize lectures:
R. Taylor, Rev. Mod. Phys. 63 (1991) 573;
H.W. Kendall, *ibid.*, p. 597; J. Friedman, *ibid.*, p. 615.
- [2] EMC: J.J. Aubert et al., Nucl. Phys. B 259 (1985) 189, *ibid.*, B 293 (1987) 740;
BCDMS: A.C. Benvenuti et al., Phys. Lett. B 223 (1989) 485, *ibid.*, B 237 (1990) 599;
NMC: P. Amaudruz et al., Phys. Lett. B 294 (1992) 120, *ibid.*, B 295 (1992) 159.
- [3] Proc. of the study for an ep facility for Europe, 1979, ed. U.Amaldi, DESY preprint 79-48 (1979).
- [4] Proc. HERA Workshop, Hamburg, 1987, ed. R.D. Peccei (DESY, Hamburg, 1988) vols. I, II.
- [5] Proc. Workshop on Physics at HERA, Hamburg, 1991, eds. W. Buchmüller and G. Ingelman (DESY, Hamburg, 1992) vols. I, II, III.
- [6] A. Jacquet and F. Blondel, in Ref. [3], p. 391.
- [7] S. Bentvelsen, J. Engelen and P. Kooijman, in Ref. [15], vol. I, p. 23.
- [8] W. Bartel et al., Proc. 4th Int. Symp. on Heavy Flavour Physics, Orsay, France, 1991, eds. M. Davier and G. Wormser (Editions Frontières, Gif-sur-Yvette, 1992) p. 515; see also Ref. [108].
- [9] I. Abt et al., this issue, Nucl. Instr. and Meth. A 386 (1997) 348.
- [10] I. Abt et al., The H1 Detector at HERA, Internal Report DESY H1-96-01, Hamburg (1996) unpublished.
- [11] B.H. Wiik, HERA status, in Ref. [5], vol. I, p. 1.
- [12] F. Willeke, in Ref. [109], p. 28.
- [13] G. Lopez et al., in Ref. [109], p. 251.
- [14] D. Pitzl et al., A silicon vertex detector for H1 at HERA, Proc. IEEE Nuclear Science Symp., Orlando, Florida, 1992; Paul-Scherrer Institut report PSI-PR-92-35, Villigen (1992).
- [15] H.J. Behrend et al., Technical proposal to build silicon tracking detectors for H1, H1 report 07/92-226, DESY, Hamburg (1992) unpublished.
- [16] UA5-Collaboration: G.J. Alner et al., Z. Phys. C 32 (1986) 153; *ibid.* C 33 (1986) 1;
R.E. Ansorge et al., Z. Phys. C 33 (1986) 175;
D.P. Johnson, Beam gas background at HERA, H1 report 07/87-65, DESY, Hamburg (1992) unpublished.
- [17] D. Decamps et al., Nucl. Instr. and Meth. A 294 (1990) 121.
- [18] P. Aarnio et al., Nucl. Instr. and Meth. A 303 (1991) 233.
- [19] Vakuumschmelze, D-6450 Hanau.
- [20] P.T.M. Clee and D.E. Baynham, Proc. 11th Int. Conf. on Magnet Technology, Tsukuba, 1989, eds. T. Sekiguchi and S. Shimamoto (Elsevier, London, 1990) p. 206.
- [21] D. Barber and J. Rossbach, Some analytical and numerical calculations of the effects of the H1 and ZEUS solenoids on the HERA optics, DESY preprint HERA 86-13, Hamburg (1986) unpublished.
- [22] ASEA Brown Boveri, CH-8050 Zürich.
- [23] W. Beckhusen et al., Proc. 12th Int. Conf. on Magnet Technology, Leningrad, 1991, IEEE Trans. Magn. 28 (1992) 801.
- [24] H. Bethe and W. Heitler, Proc. Roy. Soc. A 146 (1934) 83.
- [25] FEU-147, MELZ, Moscow, Russia.
- [26] Creative Electronics Systems SA, Fast intelligent controller FIC 8230/8232, Geneva, CH, 1987/1992.
- [27] S. Levonian, DESY preprint HERA 92-07, Hamburg (1992) 247.
- [28] C. Bini et al., Nucl. Instr. and Meth. A 306 (1991) 467.
- [29] H1 Collaboration, S. Aid et al., Z. Phys. C 69 (1995) 27.
- [30] H1 Collaboration, T. Ahmed et al., Phys. Lett. B 297 (1992) 205.
- [31] F. Sefkow et al., IEEE Trans. Nucl. Sci. NS-42 (4) (1995) 900.
- [32] S. Eichenberger et al., Nucl. Instr. and Meth. A 323 (1992) 532; see also Ref. [110], p. 214.
- [33] XILINX, The Programmable Gate Array Company, 2100 Logic Drive, San Jose, CA 95124, USA.
- [34] R. Eichler et al., The first level MWPC trigger for the H1 detector, H1 report 04/87-61, DESY, Hamburg (1987) unpublished.
- [35] T. Wolff et al., Nucl. Instr. and Meth. A 323 (1992) 537.
- [36] H.J. Behrend and W. Zimmermann, in Ref. [111], p. 237.
- [37] H. Brettel et al., Calorimeter event t_0 and trigger elements for CTL and DSP, MPI-Munich report H1-MPI-140, Munich (1990) unpublished.
- [38] F. Sefkow, Calibration of the H1 liquid argon calorimeter trigger analog thresholds, H1 report 10/94-394, DESY, Hamburg (1994) unpublished.
- [39] T. Carli et al., Performance of the H1 liquid argon calorimeter trigger in 1994, contributed paper to Int. Europhysics Conf. on High Energy Physics (EPS-HEP) EPS-0644, Bruxelles, 1995, and H1 report 07/95-455, DESY, Hamburg (1995), unpublished.
- [40] H1 BEMC group, J. Ban et al., Nucl. Instr. and Meth. A 372 (1996) 399.
- [41] J. Ban et al., The BEMC single electron trigger, H1 report 07/92-235, DESY, Hamburg (1992) unpublished.
- [42] J. Tutas, A level 1 trigger from the limited streamer tube system, H1 report 07/91-185, DESY, Hamburg (1991) unpublished.
- [43] T. Ahmed et al., Nucl. Instr. and Meth. A 364 (1995) 456.
- [44] H. Krehbiel, The H1 trigger decoder: from trigger elements to L1-keep, H1 report 09/92-239, DESY, Hamburg (1992) unpublished.
- [45] J.-C. Bizot et al., Hardware study for a topological level 2 trigger. H1 report 09/92-240, DESY, Hamburg (1992);
J.-C. Bizot et al., Status of simulation for a topological level 2 trigger, H1 report 09/92-212, DESY, Hamburg (1992) unpublished.
- [46] J. Fent et al., A level 2 calorimeter trigger using neural networks, H1 report 04/91-172, DESY, Hamburg (1991) unpublished.
- [47] E. Barrelet et al., The hardware implementation of L3 triggers in H1, H1 report 12/88-100, DESY, Hamburg (1988) unpublished.
- [48] A. Campbell, A RISC multiprocessor event trigger for the data acquisition system of the H1 experiment at HERA, Int. Conf. Real Time '91, Jülich, FRG, 1991.

- [49] S. Guenther, P. Skvaril and J. Strachota, in Ref. [110], p. 769.
- [50] R. van Staa, A slow control system for the H1 streamer tube detector, University of Hamburg II. Inst. of Physics internal report (1990), unpublished.
- [51] J. Strachota, S. Guenther and P. Skvaril. A model of minimal traffic monitoring, unpublished.
- [52] J.M. Le Goff et al., ARGUS: a graphic user interface package to monitor the slowly changing parameters of a physics experiment on a Macintosh II. CERN report ECP 91-31, Geneva (1991).
- [53] J. Pothier, BBL3, CERN report EF/L3, Geneva (1989); and private communication.
- [54] The VMEbus specification, IEEE standard 1014.
- [55] W.J. Haynes, Bus-based architectures in the H1 data acquisition system. VITA Int. Conf. Open Bus Systems '92 in Research and Industry, Zürich, Switzerland, 1992, p. 27; Rutherford Appleton Laboratory report RAL 92-048 (1992).
- [56] W.J. Haynes, in Ref. [110], p.151; DESY preprint 92-129, Hamburg (1992).
- [57] The VME Subsystem Bus (VSB) specification, IEEE standard 1096.
- [58] Creative Electronics Systems SA, RAID 8235, R3000 VMEbus controller. Geneva, Switzerland, 1990.
- [59] Creative Electronics Systems SA, VME/VSB Dual ported memory DPM 8242, Geneva, Switzerland, 1989.
- [60] B.G. Taylor, MICRON: VMEbus and CAMAC access from Macintosh, Conf. VMEbus in Research, Zürich, Switzerland (1988).
- [61] VICbus, VME Inter-Crate Bus, ISO/IEC JTC 1/SC26.
- [62] E. Pietarinen, VMEbus cross interface processor module with high speed fibre-optic links: VMExi, Univ. of Helsinki Report HU-SEFT-1991-14, Helsinki, Finland (1991).
- [63] The scalable coherent interface (SCI), IEEE standard 1596.
- [64] J. Coughlan, D. Düllmann, M. Savitski and M. Zimmer, in Ref. [110], p. 519.
- [65] W.J. Haynes, VME_TOOLS. VMEbus interaction from the MPW shell. DESY, Version 3.2, February 1994.
- [66] E. Deffur, P. Fuhrmann and M. Zimmer, Communication on the H1 local area network, H1 internal report, DESY, Hamburg (1991) unpublished.
- [67] W.J. Haynes, VMEXI_SSP: VMExi system software package. DESY, Version 4.2, July 1993.
- [68] H. Krehbiel, H1 trigger control system, H1 report 12/88-101, DESY, Hamburg (1988) unpublished.
- [69] P. Hill, MacEvLook Online version of H1 event display, DESY internal report (1991) unpublished.
- [70] P. Fuhrmann et al., Data logging and online reconstruction in H1, Proc. Int. Conf. on Computing in High Energy Physics, San Francisco, 1994, p. 482.
- [71] M. Zimmer, in Ref. [111], p. 269.
- [72] R. Gerhards et al., Experience with a UNIX based batch facility for H1. Proc. Int. Conf. on Computing in High Energy Physics, San Francisco, 1994, p. 162.
- [73] V. Blobel, Proc. 14th Workshop of the INFN Eloisatron Project: Data Structures for Particle Physics Experiments: Evolution or Revolution, Erice, Sicily, Italy, 1990, eds. R. Brun, P. Kunz and P. Palazzi (World Scientific, Singapore, 1991) p. 1.
- [74] V. Blobel, in Ref. [110], p. 755.
- [75] M. Brun, R. Brun and A.A. Rademakers, Proc. Int. Conf. on Computing in High Energy Physics, Oxford (1989), eds. R.C.E. Devenish and T. Daniels, Comp. Phys. Commun. 57 (1989) 235.
- [76] S. Egli, BOS modules in H1 software - A set of rules and recommendations H1-software note 12, DESY, Hamburg (1990) unpublished.
- [77] U. Berthon et al. A data management tool package for H1 reconstruction and analysis, H1-software note 8, DESY, Hamburg (1990) unpublished.
- [78] R. Brun et al. GEANT long write-up, CERN Program Library, W5103, 1989.
- [79] M. Kuhlen, in Ref. [112].
- [80] S. Peters, Die parametrisierte Simulation elektromagnetischer Schauer, MPI-PhE/92-13, Ph.D. thesis, University of Hamburg (1992) unpublished.
- [81] M. Rudowicz, Hadronische Schauersimulation fuer den H1 Detektor. MPI-PhE/92-14, Ph.D. thesis, University of Hamburg (1992) unpublished.
- [82] R. Brun et al., PAW long write-up, CERN Program Library. Q 121, Geneva, Switzerland.
- [83] H1 Collaboration, publication list in WWW file: http://dice2.desy.de/h1/www/publications/pub_list.html
- [84] H1 Collaboration, T. Ahmed et al., Phys. Lett. B 299 (1993) 385.
- [85] H1 Collaboration, T. Ahmed et al., Phys. Lett. B 298 (1993) 469.
- [86] H1 Collaboration, Technical proposal to upgrade the backward scattering region of the H1 detector. DESY report PRC 93-02, Hamburg (1993) unpublished.
- [87] D. Pitzl et al., Nucl. Instr. and Meth. A 348 (1994) 454. J. Bürger et al., Nucl. Instr. and Meth. A 367 (1995) 422. W. Erdmann et al., Nucl. Instr. and Meth. A 372 (1996) 188.
- [88] H1 Collaboration, Upgrade of the H1 Backward Silicon Tracker. DESY report PRC 96-02, Hamburg (1996) unpublished.
- [89] J. Bürger et al., Design of a silicon backward tracking detector and trigger for the H1 experiment at the ep collider HERA. DESY preprint 93-002, Hamburg (1993) unpublished.
- [90] H. Henschel et al., IEEE Trans. Nucl. Sci. NS-40 (4) (1993) 692.
- [91] G. Müller, A spaghetti calorimeter for the H1 detector, Proc. 5th Int. Conf. on Calorimetry in High Energy Physics, Brookhaven, 1994, p. 355.
- [92] M. Weber, The new spaghetti calorimeter of the H1 experiment, Proc. 1994 Beijing Calorimetry Symposium, Beijing, and DESY preprint 95-067, Hamburg (1995) unpublished.
- [93] H1 SpaCal group, Nucl. Instr. and Meth. A 374 (1996) 149.
- [94] H1 SpaCal group, Nucl. Instr. and Meth. A 382 (1996) 395.
- [95] H1 SpaCal group, H1 backward upgrade with a SpaCal calorimeter: the hadronic section, DESY preprint 96-013, Hamburg (1996), Hamburg (1995).
- [96] E. Eisenhandler et al., IEEE Trans. Nucl. Sci. NS-42 (4) (1995) 688.
- [97] H1 Collaboration, Technical proposal for Roman pots. DESY report PRC 93-02, Hamburg (1993) unpublished; Proposal for a forward proton spectrometer for H1, DESY report PRC 94/03, Hamburg (1994) unpublished.
- [98] J. Bähr et al., Nucl. Instr. and Meth. A 324 (1993) 145; Nucl. Instr. and Meth. A 330 (1993) 103.
- [99] J. Bähr et al., Beam tests of prototype fibre detectors for the H1 forward proton spectrometer. DESY preprint 94-130, Hamburg (1994).
- [100] D. Acosta et al., Nucl. Instr. and Meth. A 294 (1990) 193.
- [101] D. Acosta et al., Nucl. Instr. and Meth. A 314 (1991) 431.
- [102] D. Acosta et al., Nucl. Instr. and Meth. A 314 (1992) 431.
- [103] D. Acosta et al., Nucl. Instr. and Meth. A 316 (1992) 184.
- [104] M. Beck et al., Nucl. Instr. and Meth. A 381 (1996) 330.
- [105] M. Beck et al., Nucl. Instr. and Meth. A 355 (1995) 351.
- [106] G. Bernardi and W. Hildesheim, A detailed simulation of F_2 measurability at HERA. LPNHE-Paris report LPNHE-92-01 (1992); in Ref. [5], vol. I, p. 79.
- [107] D. Pitzl, Diploma thesis, University of Hamburg (1987) unpublished.
- [108] S. Egli et al., in Ref. [5], vol. II, p. 770.
- [109] Proc. 15th Int. Conf. on High-Energy Accelerators, Hamburg, 1992, ed. J. Rossbach, Int. J. Mod. Phys. A (Proc. Suppl.) 2A (1993).
- [110] Proc. Int. Conf. on Computing in High Energy Physics 92, Annecy, France, 1992, eds. C. Verkerk and W. Wojcik, CERN-Report 92-07 Geneva (1992).
- [111] Proc. Int. Conf. on Computing in High Energy Physics, Tsukuba, Japan, 1991 (Universal Academy Press, 1991).
- [112] Proc. 26th Int. Conf. on High Energy Physics, Dallas, Texas, 1992.